Numerical simulation and wind tunnel tests investigation and validation of a morphing wing-tip demonstrator aerodynamic performance

Gabor, Oliviu Şugar; Koreanschi, Andreea; Botez, Ruxandra Mihaela; Mamou, Mahmoud; Mebarki, Youssef

Publisher's version / Version de l'éditeur:
https://doi.org/10.1016/j.ast.2016.03.014
Aerospace Science and Technology, 2016-03-26

Contents lists available at ScienceDirect

Aerospace Science and Technology

www.elsevier.com/locate/aescte

Numerical simulation and wind tunnel tests investigation and validation of a morphing wing-tip demonstrator aerodynamic performance

Oliviu Şugar Gabor [a], Andreea Koreanschi [a], Ruxandra Mihaela Botez [a], Mahmoud Mamou [b], Youssef Mebarki [b]

[a] LARCASE Laboratory of Applied Research in Active Control, Avionics and Aeroservoelasticity, Ecole de Technologie Superieure, Montreal, Que., H3C1K3, Canada
[b] Aerodynamics Laboratory, NRC Aerospace, National Research Council Canada, Ottawa, Ont., K1A0R6, Canada

ARTICLE INFO

Article history:
Received 27 November 2015
Received in revised form 20 March 2016
Accepted 21 March 2016
Available online xxxx

Keywords:
Morphing wing
Morphing aileron
CFD
Infra-red tests
Wind tunnel tests
Laminar-to-turbulent flow transition

ABSTRACT

This paper presents the results obtained from the numerical simulation and experimental wind tunnel testing of a morphing wing equipped with a flexible upper surface and controllable actuated aileron. The technology demonstrator is representative of a real aircraft wing tip section, and it was developed following a complex, multidisciplinary design process. The model was fitted with a composite material upper skin whose shape can be morphed, as a function of the flight condition, by four electrical actuators placed inside the wing structure. The optimizations were performed with the aim of controlling the extent of the laminar flow region, and the resulting shapes were scanned using high-precision photogrammetry. The numerical simulations were performed using Computational Fluid Dynamics (CFD) and included a model for predicting the laminar-to-turbulent flow transition over the entire wing surface. The analyses included cases with three aileron deflection angles and angles of attack situated within five degrees range. The CFD results were compared with infrared thermography measurements in terms of transition location, surface pressure measurements and balance loads measurements acquired during subsonic wind tunnel tests performed at the National Research Council Canada.

1. Introduction

The air transportation industry is a key contribution to economic development around the world. Since the beginning of civil aviation, there has been a steady increase in the number of passengers using airplanes as a fast and safe transportation method, with airlines carried almost three billion passengers worldwide in 2014 alone. This high level of development that has been achieved has also transformed the air transport industry into a non-negligible source of pollution. It is estimated that in 2014, over 2% of the worldwide carbon dioxide emissions were attributed to commercial airline companies [1].

The current growth rate is anticipated to accelerate over the next several decades. The International Civil Aviation Organization (ICAO) estimates that the number of flights will triple by the year 2050 [2]. This growth rate, together with growing global concern for the preservation of the environment and the reduction of greenhouse gas emissions is forcing the aerospace industry to search for solutions to improve aircraft fuel burn efficiency.

One possibility of achieving this desired efficiency is through the new-generation technologies of morphing various aircraft lifting surface, that can be activated and deformed according to the flight conditions, thus allowing a multi-point design of the aircraft and improving aerodynamics performance. A morphing wing could allow the aircraft to fly at optimal lift-to-drag ratios for any condition encountered during flight by changing some of the wing's characteristics. Researchers have proposed different technological solutions for obtaining the desired wing adaptability, and some concepts have achieved important theoretical performance improvements compared to the baseline design. However, the technology is still in the early stages of development, its technological readiness level is still low, and only a few concepts have sufficiently progressed to reach wind tunnel testing, and even fewer have actually been flight tested [3].

Wing morphing techniques can be classified into three major types: plan-form transformations (sweep angle, span and chord), out-of-plane transformations (twisting, dihedral and spanwise bending) and airfoil transformations (camber and thickness) [3].

E-mail address: ruxandra.botez@etsmtl.ca (R.M. Botez).

http://dx.doi.org/10.1016/j.ast.2016.03.014
1270-9638/© 2016 Published by Elsevier Masson SAS.

Morphing wings were used to adapt the wing span and airfoil camber [4,5] or the winglet's cant and toe angles [6], and to replace conventional high-lift devices [7,8], or the conventional control surfaces [9].

Lockheed Martin developed the Agile Hunter Unmanned Aerial Vehicle (UAV) [10–12], capable of folding the inner region of the wing over the fuselage in order to achieve drag reductions during transonic cruise at lower altitudes. A morphing wind tunnel prototype was built and tested up to a Mach number of 0.6. The model demonstrated a successful and accurate actuation under aerodynamic loads, achieving the desired wing shape change in approximately one minute. An important project for the development of morphing wings was the NexGen Aeronautics MFX1 UAV, showing wing sweep and chord changes [13,14]. The wing was based on a morphing truss structure that could be controlled using electrical actuators. A prototype of the UAV was built and successfully flight tested. The morphing wing sustained sweep angle variations of 20° and area changes of 40% under aerodynamic loading, for flight speeds up to 100 knots.

A detailed computational and experimental analysis was performed by Smith et al. [15] on the wing of a conventional aircraft equipped with two outboard morphing partitions capable of varying the twist and the dihedral angles. The morphing system was capable of providing twist variations of up to 3°, and dihedral variations of up to 90°. Researchers from NASA Dryden Flight Research Center conducted several flight tests with a UAV equipped with inflatable wings whose span could be modified by adjusting the pressure input [16]. The wings were made from several spanwise inflatable tubes, surrounded by sponge and a flexible nylon skin in order to maintain the airfoil shape during flight. A variable wing plan-form UAV was designed and tested by Neal et al. [17]. The system used pneumatic actuators to drive the telescopic and rotating wing, capable of achieving significant wing span and sweep angle changes. Wind tunnel tests were performed and showed that only three morphing wing configurations were needed to significantly increase the lift-to-drag ratio for the entire flight envelope of the UAV.

Pecora et al. [18] demonstrated the effectiveness of replacing the conventional segmented flap with a morphing compliant high-lift device, in the case of a regional transport aircraft. Bilgen et al. [19,20] also presented the concept of replacing the wing trailing-edge devices with a morphing surface, capable of achieving continuous camber variations instead of rigid deflections. The morphing system was designed to replace the ailerons of a UAV, and thus used rapid, electrical actuation mechanisms. Both wind tunnel experiments and preliminary flight test were performed, and demonstrated the effectiveness of the concept at providing accurate roll control. Pankonien and Inman [21] presented a concept for morphing ailerons designed to replace the conventional wing control surfaces of a UAV. The aerodynamic performance of the system was evaluated using wing tunnel testing, with measurements focused on the drag coefficient penalty associated with classic control surface deflections at off-design flight conditions. The morphing trailing edge achieved drag reductions of up to 20% compared to the original design, thus justifying its increased mass and complexity.

The CRIAQ 7.1 project, which took place between 2006 and 2009, was realized following a collaborative effort between teams from the École de Technologie Supérieure (ÉTS), École Polytechnique de Montréal, Bombardier Aerospace, Thales Canada and the National Research Council Canada (CNRC). The objective of the project was to improve and control the laminarity of the flow past a morphing wing in order to obtain a substantial drag reduction [22].

In that project, the active structure of the morphing wing consisted of three main subsystems: a flexible skin; a composite material upper surface spanning between 3% and 70% of the airfoil chord, a rigid inner surface and a Shape Memory Alloy (SMA) actuator group located inside the wing box, which could morph the flexible skin at two actuation points, located respectively at 25.3% and 47.6% of the chord [23]. The reference airfoil chosen for the project was the WTEA laminar airfoil and the morphing system was designed for low subsonic flow conditions. A theoretical study of the morphing wing system was performed [24], and very promising results were obtained: the morphing system was able to delay the transition location downstream by up to 30% of the chord, and to reduce the airfoil drag by up to 22%.

Two control approaches were used for providing the optimal SMA actuator displacements for each different flight condition. In the open-loop configuration, the desired displacements were directly imposed on the system [25], while a novel, adaptive, neuro-fuzzy approach which was used to predict and control the morphing wing performance [26]. In the closed-loop configuration, the displacements were automatically determined as a function of the pressure readings from the wing upper surface [27,28]. In addition, two new controllers were developed; the first one was based on an optimal combination of the bi-positional and Proportional-Integral (PI) laws [29,30], while the second one was a hybrid fuzzy logic-PID controller [31,32]. The wind tunnel tests were performed in the 2 m × 3 m atmospheric closed circuit subsonic wind tunnel at NRC. The wind tunnel measurements were analyzed to assess the validity of the numerical wing optimizations [33] and the designed control techniques [34].

2. Description of the CRIAQ MDO 505 project

2.1. Project information

The CRIAQ MDO 505 project is performed as a continuation of the CRIAQ 7.1 project on adaptive upper-surface wing concept. In this multidisciplinary project a real industrial wing and aileron (classical and morphing) structure was considered and designed following structural and materials optimizations based on new aerodynamic optimization constraints and new morphing skin control challenges, using an electrical actuation system along with classical and adaptive ailerons.

The research presented in this paper was performed within the framework of the MDO 505 project, a multiple partners project involving an international collaboration between Canadian and Italian industries, universities and research centers (Bombardier Aerospace, Thales Canada and Alenia Aeronautica, on the industry side, École de Téchnologie Supérieure, École Polytechnique de Montreal and the University of Naples, on the academic side, and NRC and the Italian Institute for Aerospace Research CIRA on the research centers side).

The purpose of the CRIAQ MDO 505 project is to demonstrate the structural, aerodynamic and control abilities of a wind tunnel wing model equipped with an adaptive upper surface and both a rigid and an adaptive aileron, designed for low-speed (subsonic) wind tunnel tests. The novelty of this project consists in the multidisciplinary design, analysis and manufacturing of a wind tunnel representative model that respects the structural and aerodynamic properties of a real aircraft wing-tip section. The morphing wing model structure was designed to closely follow the real aircraft wing-tip section dimensions, while allowing the insertion of the actuation system. Reynolds number similitude of the morphing wing model with the real aircraft was achieved for the low-speed aerodynamic tests by using the same spanwise chord distribution as the one real wing-tip section, and maintaining the same mean aerodynamic chord. Fig. 1 presents the position of the morphing upper skin on a typical aircraft wing, while Fig. 2 presents the structural elements of the morphing wing model.

Please cite this article in press as: O. Şugar Gabor et al., Numerical simulation and wind tunnel tests investigation and validation of a morphing wing-tip demonstrator aerodynamic performance, Aerosp. Sci. Technol. (2016), http://dx.doi.org/10.1016/j.ast.2016.03.014

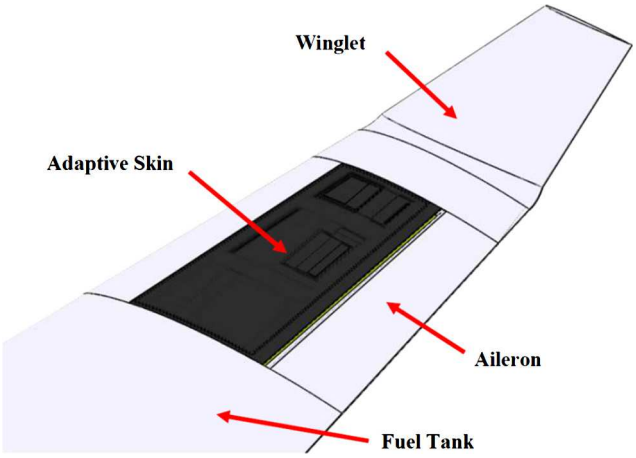

Fig. 1. The layout of the morphing skin on the aircraft wing.

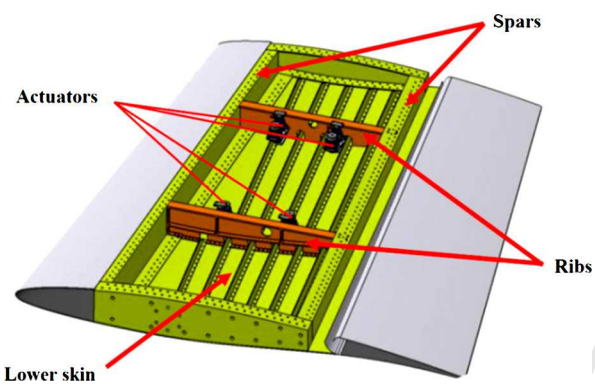

Fig. 2. The structural elements of the CRIAQ MDO 505 morphing wing concept (the morphing skin is not shown in the figure).

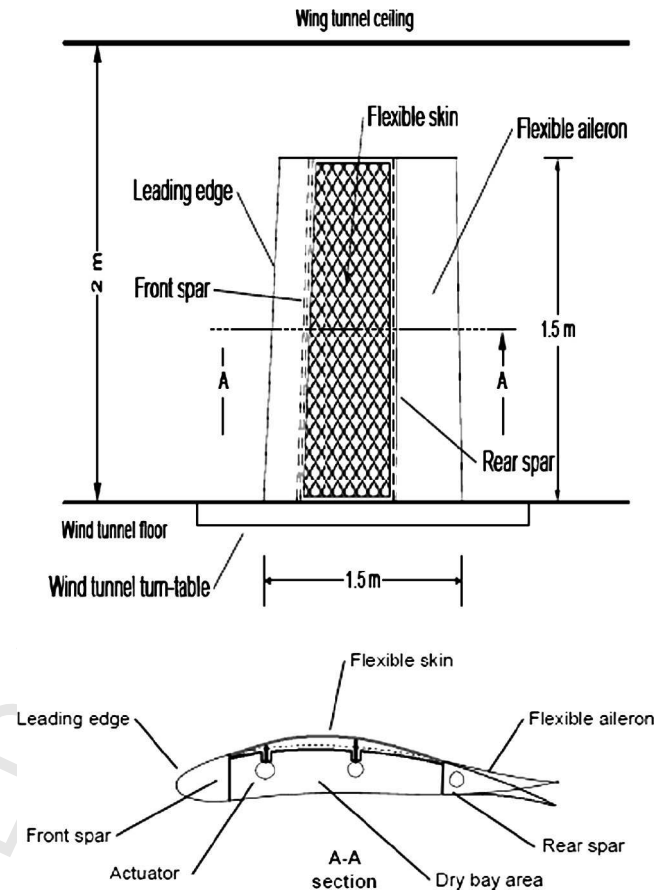

Fig. 3. CRIAQ MDO 505 morphing wing concept.

2.2. General details about the morphing wing model

The full-scale morphing wing model is a structure with a 1.5 m span and a 1.5 m root chord, a taper ratio of 0.72, and leading and trailing edges sweep angles of 8°. The chord distribution of the wing model follows the chord distribution of the real wing-tip section, while the sweep angle and the spanwise twist distribution were modified in order to reduce 3D flow effects. The wing box and its internal structure (spars, ribs, and lower skin) were manufactured from aluminum alloy material, while the adaptive upper surface was positioned between 20% and 65% of the wing chord. The adaptive upper surface skin was specifically designed and optimized for the project, and was manufactured using carbon fiber composite materials [35].

The deformation of skin shape, driven by actuators placed inside the wing box structure, is a function of the flight condition (defined in terms of Mach number, Reynolds number and angle of attack). These actuators were specifically designed and manufactured to meet the project requirements. Four electric actuators were installed on two actuation lines; two actuators each, placed at 37% and 75% of the wing span, fixed to the ribs and to the composite skin. Each actuator has the ability to operate independently from the others, and has a displacement range between ±3.5 mm. On each actuation line, the actuators were positioned at 32% and 48% of the local wing chord.

The aileron articulation was located at 72% of the chord. Two ailerons were designed and manufactured. One aileron was structurally rigid, while the other one represented a new morphing aileron concept. Both ailerons were designed to be attached to the same hinge axis of the wing box, and both are able to undergo a controlled deflection between −7° and +7°. This interval is more restricted than the normal deflection range of an aileron, but it was considered sufficient to demonstrate the proof of concept for the morphing aileron. This restriction was determined by the available space inside the NRC wind tunnel and by the mechanical design of the morphing mechanism. Fig. 3 presents a sketch of the morphing wing model concept as it would be mounted and tested in the NRC subsonic wind tunnel.

2.3. The structural design of the morphing wing model

The MDO 505 morphing wing was designed to have a structural rigidity similar to a real aircraft wing-tip. This means that when the wing model was subjected to in-flight 1g loads, the bending moment, the torsional moment and the shear stresses at the ribs were similar to those obtained for the real aircraft wing-tip. The upper surface morphing skin was created not only to be an active structural element, rigidly fixed around its perimeter and able to withstand real flight loads, but also to allow the obtaining of the required aerodynamic shape changes and actuator displacements while remaining structurally loaded.

Two Finite Element Models (FEMs) were created for the design process: a simplified, thus general model (GFEM) that was used to design and optimize the carbon fiber upper surface skin, and a detailed model (DFEM) that was used for the design and numerical analysis of the rigid structure (lower skin, spars, ribs, internal actuators). The FEM's were created using the Altair Hyperworks software package, while NASTRAN was used as the FEM solver. The aerodynamic loads used for dimensioning and calculating the structural elements of the morphing wing model correspond to the limit load factors of +2.5g and −1g typical of civil transport aviation, multiplied by the ultimate security coefficient of 1.5 [35].

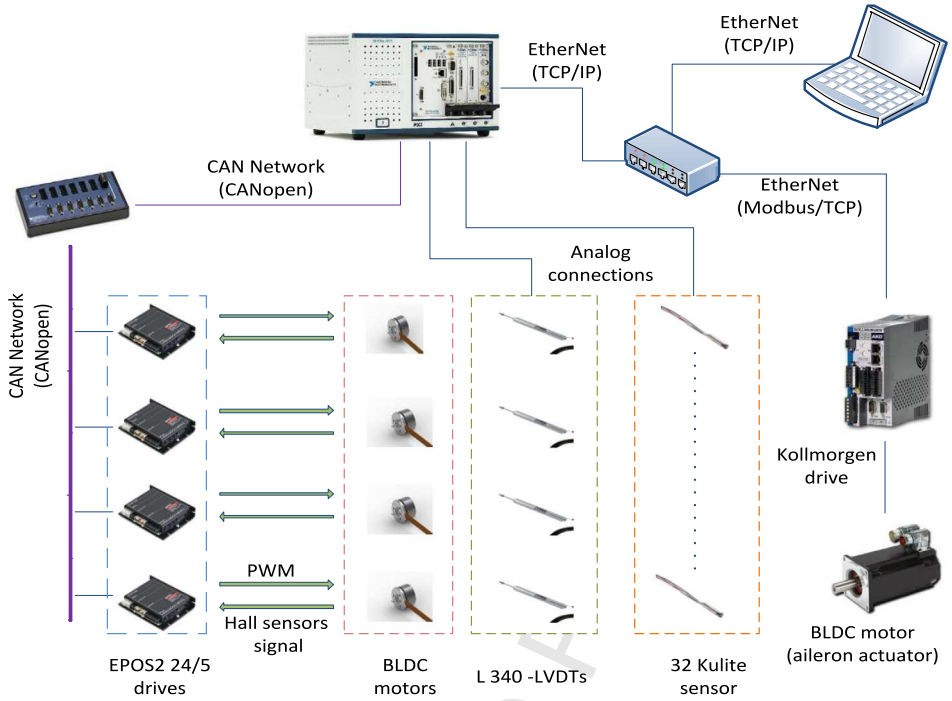

Fig. 4. Overview of the morphing wing control system.

For the leading edge, lower skin and ribs, the GFEM was generated using 2D CQUAD4 and CTRIA3 elements, having the PSHELL property. The flexible upper skin 2D elements had the PCOMP property attributed. The spars and stringers were modeled with 1D BEAM elements, having the PBEAML property. The complete GFEM model had approximately 180000 elements. The DFEM comprised almost 4 million elements, allowing to perform a more detailed numerical simulation. A mixture of 1D, 2D and 3D elements (CTETRA having the PSOLID property) was used, while both upper and lower skins were modeled using only 2D CQUAD4 and CTRIA3 elements, but with much higher mesh density than the GFEM [35].

The flexible skin design and optimization were performed using the Altair Optistruct solver, while trying to match structurally as close as possible the aerodynamically optimized upper surface shapes [35]. The optimization approach was done in three stages. The *free-size optimization* focused on determining the global thickness of the skin and of the composite plies. The *dimensional optimization* refined the plies thicknesses as function of their orientation and topography. The *final stage* was the optimizations of the plies layout as function of manufacturing constraints.

An error analysis performed for a number of optimized cases showed that the average shape error between the skin FEM and the spline target shapes was 0.25 mm, or 7% of the maximum actuator displacement. Given the multidisciplinary nature of the MDO 505 project and the high number of structural requirements on the carbon fiber skin, a good reproduction of the desired optimized shapes was numerically obtained using the FEM analysis.

2.4. The wing model control system

The core of the wing control system was the embedded real time controller PXI-e 8135 of National Instruments. This controller ran on a real time operating system, and was connected to all the system hardware peripherals through several input and output modules. All four upper skin actuators (BLDC motors), the rigid aileron actuator, the LVDT sensors for providing the actuators positions feedback, as well as the upper skin Kulite pressure sensors were connected to the PXI-e 8135 system. The controller was monitored by the host PC via an Ethernet network using the TCP/IP communication protocol, which had a static IP address that was personalized and fixed by the system operator. The Windows OS machine (the host PC) served for the control program deployment, system state control, and data monitoring in real time. All communication tasks, control and data logging were entirely operated by the PXI-e 8135, which ran independently of the host PC. Fig. 4 presents an overview of the integrated controller and data monitoring system of the morphing wing model.

3. Flow equations, turbulence and transition models

CFD simulations were performed to simulate the flow past the wing under the wind tunnel test flow conditions and set up. The dynamics of fluid flow are governed by the Navier–Stokes equations, which represent the fundamental principles of mass, momentum and energy conservation. For turbulent flows, the Reynolds Averaging technique is used to decompose the instantaneous flow variables into their average values and turbulent fluctuations, while the Boussinesq eddy-viscosity hypothesis is used to relate the Reynolds stress tensor and turbulent heat flux terms to the average flow variables. With these assumptions, the Reynolds Averaged Navier–Stokes (RANS) equations (with Reynolds average flow variables) can be written as follows:

$$\frac{\partial \rho}{\partial t} + \frac{\partial}{\partial x_j}(\rho U_j) = 0 \tag{1}$$

$$\frac{\partial}{\partial t}(\rho U_i) + \frac{\partial}{\partial x_j}(\rho U_j U_i) = -\frac{\partial P}{\partial x_i} + \frac{\partial}{\partial x_j}\left[\mu_{eff}\left(\frac{\partial U_i}{\partial x_j} + \frac{\partial U_j}{\partial x_i}\right) - \frac{2}{3}\mu_{eff}\frac{\partial U_k}{\partial x_k}\delta_{ij}\right] \tag{2}$$

$$\frac{\partial}{\partial t}(\rho H) - \frac{\partial P}{\partial t} + \frac{\partial}{\partial x_j}(\rho U_j H) = \frac{\partial}{\partial x_j}\left[\lambda\frac{\partial T}{\partial x_j} + \frac{\mu_t}{Pr_t}\frac{\partial h}{\partial x_j}\right] + \frac{\partial}{\partial x_j}\left\{U_i\left[\mu_{eff}\left(\frac{\partial U_i}{\partial x_j} + \frac{\partial U_j}{\partial x_i}\right) - \frac{2}{3}\mu_{eff}\frac{\partial U_k}{\partial x_k}\delta_{ij}\right] + \mu\frac{\partial k}{\partial x_j}\right\} \tag{3}$$

where ρ is the fluid density, U_i are the velocity components, P is the sum of the static pressure and the $(2\rho\delta_{ij}k)/3$ term resulting from the Boussinesq assumption, μ_{eff} is the effective viscosity, given by the sum of the molecular viscosity μ and the turbulent viscosity μ_t, δ_{ij} is the Kronecker delta function, H is the total enthalpy, T is the fluid temperature, λ is the thermal conductivity, Pr_t is the turbulent Prandtl number, h is the static enthalpy and k is the turbulent kinetic energy.

The turbulent viscosity and the kinetic energy are determined using the k–ω Shear Stress Transport (SST) model [36]. The SST model represents a blend of the k–ω model, used in the near wall region, and the k–ε model, used for the rest of the flow. Thus, it achieves both accurate boundary layer representation up to the viscous sub-layer and insensitivity to boundary conditions at free-stream flow. The SST turbulence model equations are presented below:

$$\frac{\partial}{\partial t}(\rho k) + \frac{\partial}{\partial x_j}(\rho U_j k) = P_k - D_k + \frac{\partial}{\partial x_j}\left[(\mu + \sigma_k \mu_t)\frac{\partial k}{\partial x_j}\right] \tag{4}$$

$$\frac{\partial}{\partial t}(\rho\omega) + \frac{\partial}{\partial x_j}(\rho U_j \omega) = \frac{\gamma}{\mu}P_k - \beta\rho\omega^2 + \frac{\partial}{\partial x_j}\left[(\mu + \sigma_\omega \mu_t)\frac{\partial \omega}{\partial x_j}\right] + 2(1-F_1)\rho\sigma_{\omega 2}\frac{1}{\omega}\frac{\partial k}{\partial x_j}\frac{\partial \omega}{\partial x_j} \tag{5}$$

where k is the turbulent kinetic energy, P_k is the turbulent kinetic energy production term, D_k is the turbulent kinetic energy destruction term, ω is the specific turbulence dissipation rate, F_1 is a blending function related to the SST model, and γ, β, σ_k, σ_ω and $\sigma_{\omega 2}$ are the constants of the model. The turbulent viscosity is calculated as:

$$\mu_t = min\left(\frac{\rho k}{\omega}, \frac{a_1 \rho k}{S F_2}\right) \tag{6}$$

where a_1 is a damping coefficient, S is the strain rate magnitude and F_2 is a second blending function related to the SST model.

In order to include the effects of laminar flow and model the laminar-to-turbulent transition process, the γ–$Re_{\theta t}$ model is used [37]. This model includes two more equations, one for the intermittency and one for the transition momentum thickness Reynolds number:

$$\frac{\partial}{\partial t}(\rho\gamma) + \frac{\partial}{\partial x_j}(\rho U_j \gamma) = P_\gamma - E_\gamma + \frac{\partial}{\partial x_j}\left[\left(\mu + \frac{\mu_t}{\sigma_f}\right)\frac{\partial \gamma}{\partial x_j}\right] \tag{7}$$

$$\frac{\partial}{\partial t}(\rho\overline{Re_{\theta t}}) + \frac{\partial}{\partial x_j}(\rho U_j \overline{Re_{\theta t}}) = P_{\theta t} + \frac{\partial}{\partial x_j}\left[\sigma_{\theta t}(\mu + \mu_t)\frac{\partial \overline{Re_{\theta t}}}{\partial x_j}\right] \tag{8}$$

where γ is the intermittency, P_γ is the intermittency production term, E_γ is the intermittency destruction/relaminarization term, $\overline{Re_{\theta t}}$ is the transition momentum thickness Reynolds number, $P_{\theta t}$ is the transition momentum thickness Reynolds number production term, and σ_f and $\sigma_{\theta t}$ are model constants.

The transition onset is controlled by an empirical correlation between $Re_{\theta c}$, the critical Reynolds number where the intermittency starts to increase in the boundary layer, and $\overline{Re_{\theta t}}$ [37]. The model contains correction terms to account for laminar separation-induced transition and strong pressure-gradient flows. Coupling of the γ–$Re_{\theta t}$ transition model with the k–ω SST turbulence model is done by modifying P_k and D_k, the turbulent kinetic energy production and destruction terms, and thus deactivating the turbulence model for the laminar boundary layer region.

The numerical computations were performed with the ANSYS FLUENT solver [38]. The steady-state flow equations were solved using a projection method, achieving the constraint of mass conservation by solving the pressure equation, with the pressure-velocity coupling accomplished by using a high-order Rhie–Chow scheme. The cell-face values of the pressure were interpolated using a second-order central differencing scheme, while for all other variables, including the turbulence and transition model equations, a second-order upwind scheme was used. The discrete nonlinear equations were solved in a fully implicit, coupled manner. Convergence acceleration was achieved with a coupled algebraic multigrid (AMG) approach, using a block-method Incomplete Lower–Upper (ILU) factorization scheme as the linear system smoother.

4. Morphed geometries and mesh generation

4.1. The theoretical optimized upper surface shapes

The core concept of an active morphing of the wing upper surface is to provide an optimized airfoil shape for each flight condition. A single point optimization must be performed for each combination of Mach number, Reynolds number and angle of attack. This procedure increases the aerodynamic performance of the shape-changing airfoil (with respect to the desired optimization objective) compared to the multi-point designed baseline airfoil.

Aerodynamic optimizations were performed to determine the actuator-driven displacements required to improve the performance of the morphing wing with respect to the original wing. In order to reduce greatly calculation times, the aerodynamic optimizations were performed under two-dimensional flow assumption using the XFOIL solver [39] and an in-house genetic algorithm optimizer [40], for local flow conditions (local Reynolds number and angle of attack) corresponding to the mean aerodynamic chord of the wing model [41].

For the numerical optimizations, the upper skin shapes were approximated using cubic splines, as function of the actuator displacements. This mathematical model was chosen because it enforces the tangency condition with the rigid part of the airfoil (up to the curvature continuity given by the second derivative), it provides an iso-arc-length condition and it shares mathematical properties with a beam bending under an applied load. Due to constraints related to structural rigidity of the composite skin, the actuator displacements were limited to ±3.5 mm, while the maximum difference between the two displacements was limited to 6 mm.

4.2. Measurement of the real upper surface shapes

Due to the high degree of multidisciplinary involved in the development of the MDO 505 morphing wing project, the contradictory requirements that the morphing upper surface had to satisfy (rigid in order to withstand flight loads, but at the same time flexible enough to allow proper controlled deformations) and the very high precision required for the aerodynamic optimization, it was decided to scan the shapes obtained after the completion of the manufacturing process. This way, the simulations would be performed on geometries that were practically achieved, and not on surfaces reconstructed using mathematical modeling.

To construct the geometries required for the 3D calculations, the real shapes of the morphing skin surface for all flight cases were scanned using a high precision photogrammetry procedure, utilizing three 3D-tracking cameras (Prime 41 from Natural Point) [42]. Circular retro-reflective markers were applied on the wing upper surface, and their positions were recorded for each skin shape. Fig. 5 presents the marker positions for the un-deformed skin, as measured with the scanning procedure. The estimated maximum position error with this procedure is 0.07 mm, using the known positions of the four actuators axes.

Please cite this article in press as: O. Şugar Gabor et al., Numerical simulation and wind tunnel tests investigation and validation of a morphing wing-tip demonstrator aerodynamic performance, Aerosp. Sci. Technol. (2016), http://dx.doi.org/10.1016/j.ast.2016.03.014

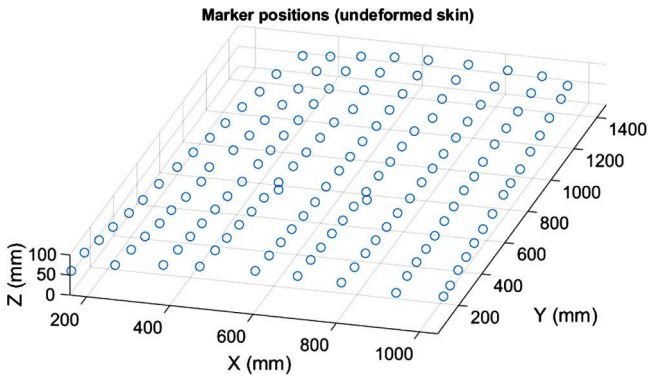

Fig. 5. Marker positions for the un-deformed upper skin.

To increase the resolution of the scanned data, a bi-harmonic spline interpolation procedure was performed between the marker positions, and the number of points was increased to 100 in both chord-wise and span-wise directions. Fig. 6 presents the 100×100 grid points obtained by interpolation for the un-deformed skin (upper image), and the deformed shape of the flexible skin for the C41 configuration (lower image).

The procedure of determining the marker positions through the photogrammetry technique and then interpolating using splines to increase the density of surface points was repeated for all of the morphing cases. The data was further used to construct the geometries required for the 3D calculations by patching the upper surface skin shapes on the rigid geometry representing the rest of the wing model. An accurate representation of the real skin shapes was therefore available for performing the numerical simulations.

4.3. Comparison between target and obtained shapes

Following the reconstruction of the morphed wing geometries using the scan data, comparisons were performed between the target skin shapes (obtained after the aerodynamic optimization process) and the real skin shapes. Fig. 7 presents the comparison between the target and obtained shapes for Case 75.

The comparison was made at four stations along the wing span, located at 0.55 m, 0.75 m, 0.95 m and 1.15 m, as measured from the wing root section. The first and the last section correspond to the positions of the two ribs where the electrical actuators were installed. From Fig. 7 it can be seen that for these two sections there is an excellent agreement between the target shapes obtained from the numerical optimization and the obtained skin shapes. The other two sections correspond to positions between the two ribs. For these sections, there is a more significant difference between the desired and the scanned shapes. At certain points, this difference can reach magnitudes of approximately 2 mm, thus an important percentage of the maximum displacement range of the electrical actuators (±3.5 mm).

Since the three-dimensional numerical study is performed using the scanned upper surface shapes, this difference does not have an impact on the numerical versus experimental comparisons in terms of laminar-to-turbulent transition location. However, the performance of the morphed geometries with reference to the original, un-deformed wing is expected to be smaller than predicted, since the targeted optimal shapes are not obtained for the entire wingspan.

4.4. Grid convergence study

The structured meshes used for the numerical simulation were generated using the ICEM-CFD software. A grid convergence study was performed in order to evaluate the mesh density required for

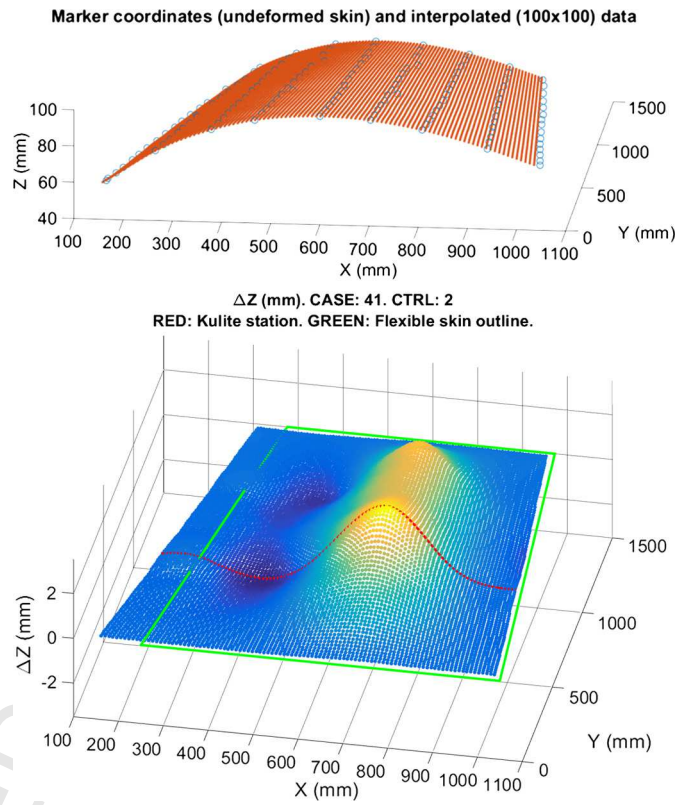

Fig. 6. Interpolated point grid constructed from the scanned marker positions for the un-deformed upper skin (upper) and the Case 41 morphed upper surface (lower). (For interpretation of the references to color in this figure, the reader is referred to the web version of this article.)

Table 1
Details about the four generated meshes.

Mesh type	Chord-wise cells on wall	Span-wise cells on wall	Maximum $y+$
Coarse	100	40	2.66
Medium	200	80	1.33
Fine	400	160	0.66
Extra fine	800	320	0.33

grid-independent aerodynamic coefficients values. Four meshes of increasing cell density were generated, and each one was analyzed at a Mach number of 0.15, a Reynolds number of 4.53E+06 (as calculated with the wing mean aerodynamic chord) and an angle of attack of 0°. The details regarding the wall cell density for the generated meshes are presented in Table 1.

The wing aerodynamic coefficients values (lift, drag and pitching moment coefficient about the root section quarter chord point) and the transition point locations on the upper surface, at 37% and 75% of the span stations are presented in Table 2. The transition point locations were determined using the intermittency variable γ distribution. The table shows that the difference in aerodynamic coefficient values between the Fine mesh level and the Richardson extrapolation of the convergence study is less than 1%, and thus the Fine mesh provides sufficiently accurate results. It can be observed that the γ–$Re_{\theta t}$ model requires a good stream-wise mesh refinement level before the grid convergence of the transition point location is achieved (thus also affecting the grid convergence of the drag coefficient, through the variation of the laminar flow region length).

The characteristics of the meshes used to perform the simulations were determined based on the results of the grid convergence study. In order to ensure that the same meshing parameters

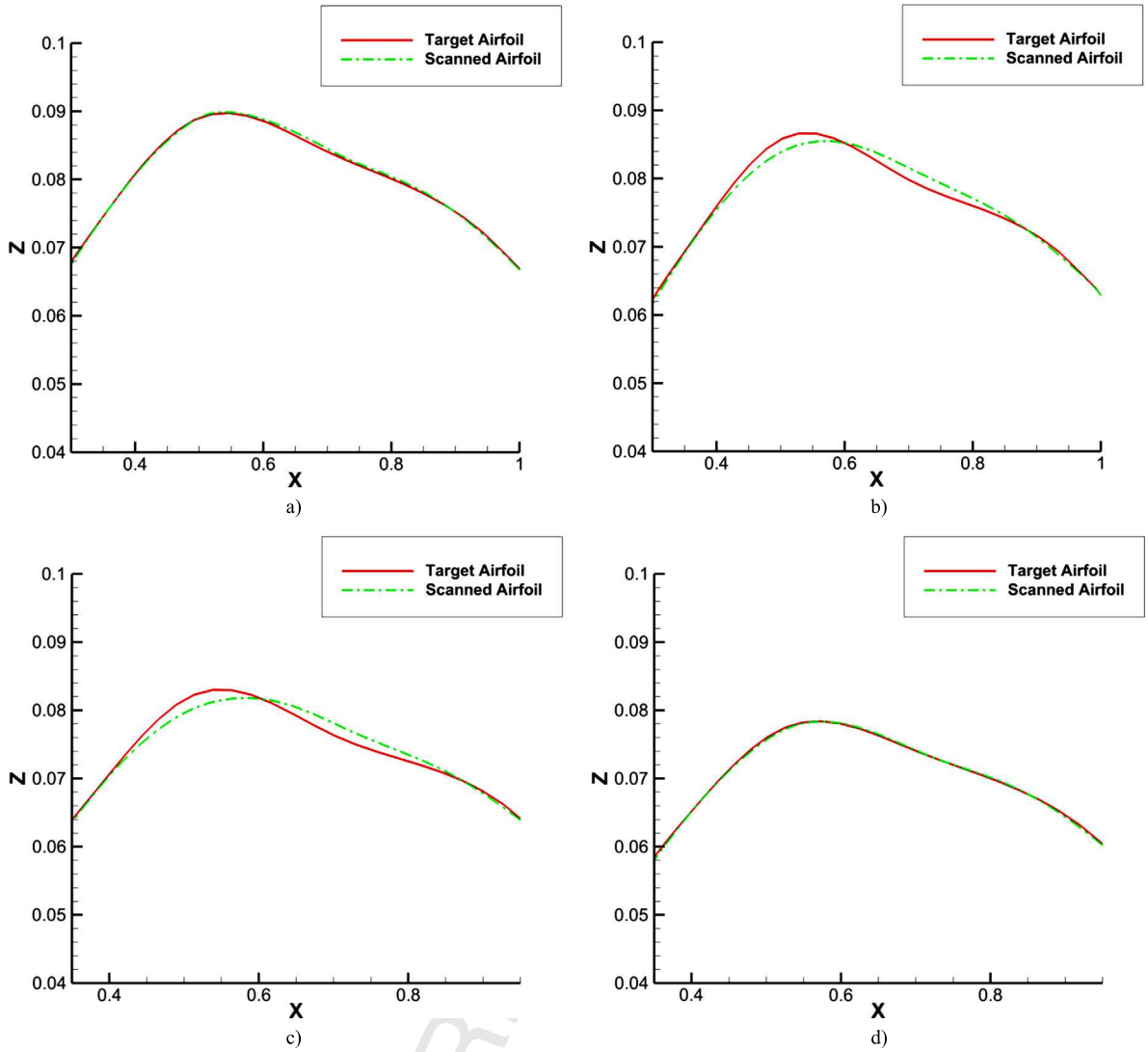

Fig. 7. Comparisons between the upper surface skin shapes of the target airfoil and of the scanned airfoil, at four stations along the wingspan: $Y = 0.55$ m (a), $Y = 0.75$ m (b), $Y = 0.95$ m (c) and $Y = 1.15$ m (d).

Table 2
Results obtained for the grid convergence study.

Mesh type	CL	CD	Cm	Transition at 37% of span (% of local chord)	Transition at 75% of span (% of local chord)
Coarse	1.531E–01	1.308E–02	−9.235E–02	13.4%	3.4%
Medium	1.587E–01	9.855E–03	−9.264E–02	48.2%	32.8%
Fine	1.593E–01	9.621E–03	−9.273E–02	57.5%	36.9%
Extra fine	1.596E–01	9.609E–03	−9.274E–02	58.0%	37.1%
Richardson extrapolation	1.597E–01	9.605E–03	−9.276E–02	58.2%	37.1%

were used for all the morphed wing cases, an automatic mesh generation procedure was implemented by creating a script to be used for the ICEM-CFD code. The automatic procedure can also handle rigid aileron deflections between ±7°. The meshes were constructed based on the Fine mesh level created for the convergence study, and include 400 cells around the wing section (200 cells on both the lower and upper surfaces), and 160 cells in the direction of the span (80 cells on both the lower and upper surfaces). The wall normal spacing was set to 3.0E–06 m, refined enough to provide the required $y+ < 1$ condition. Figs. 8 and 9 present two cross-section views of the mesh constructed around the unmorphed wing.

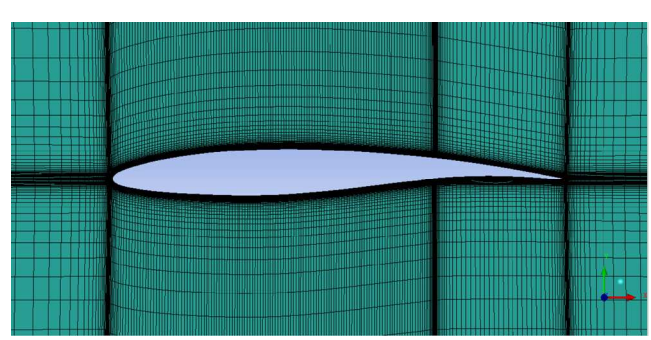

Fig. 8. Chord-wise cross-section view of the mesh.

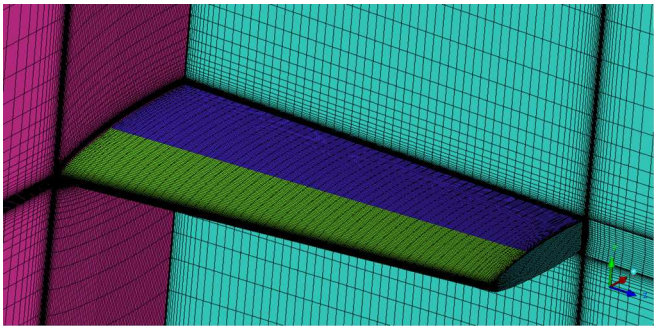

Fig. 9. Spanwise cross-section view of the mesh.

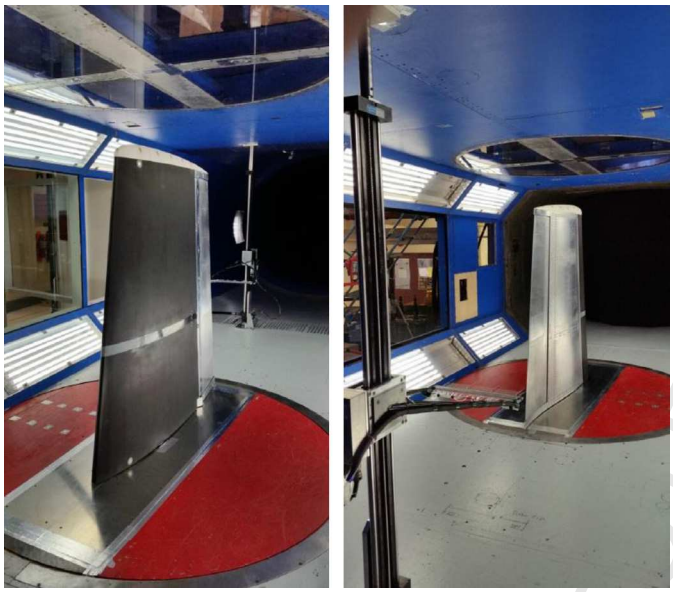

Fig. 10. MDO 505 wing model setup in the wind tunnel test section.

5. Experimental testing and data acquisition

The wind tunnel tests were performed at the 2 m × 3 m atmospheric closed circuit subsonic wind tunnel of the National Research Council Canada. The tunnel has a maximum speed corresponding to a Mach number of 0.40, at atmospheric pressure.

The upper surface flexible skin was equipped with 32 high precision Kulite piezoelectric-type transducers [43] for pressure measurement on the flexible skin and then processed to determine the laminar-to-turbulent transition location. These sensors were installed in two staggered lines (with 16 Kulite sensors on each line), situated respectively at 0.600 m and 0.625 m from the wing root section. In addition to the Kulite piezoelectric sensors, at the same two spanwise stations, 60 static pressure taps were installed (30 taps on each line), on the wing leading edge, lower surface and aileron, thus providing complete experimental pressure distribution around the wing cross section at 40% of the wing span.

The experimental measurements also included the use of a wake rake pressure acquisition system, to measure the wing profile drag at different span-wise positions, and the use of a wind tunnel balance for measuring the aerodynamic forces and moments. Fig. 10 presents the MDO 505 morphing wing model installed in the tunnel test section, viewed from both the leading edge (left figure) and the trailing edge (right figure).

Infra-red (IR) thermography camera visualizations were performed for capturing the transition region over the entire wing model surface. The wing leading edge, its upper surface flexible skin and the aileron interface were coated with high emissivity black paint to improve the quality of the IR photographs. The span-wise stations where the two pressure sensors lines were installed were not painted, in order to not influence the pressure measurements. A Jenoptik Variocam camera [44], with a resolution of 640 by 480 pixels, was used to measure the surface temperatures. This camera was equipped with 60° lens in order to capture the flow transition on the entire upper surface of the wing. A custom wooden window was installed on the wind tunnel test section wall, through which the IR camera operated.

The IR thermography visualization allows the identification of the laminar-to-turbulent transition region based on the temperature gradient between the two flow regimes, which is determined by the different convective heat transfer coefficients and heat flux dissipation existing in the two regimes when the surface is heated to a fixed temperature. Fig. 11 presents an example of the IR visualization of the wing model upper surface transition, for one flight condition (Mach number of 0.15, angle of attack of 1° and no aileron deflection) and for both un-morphed (left figure) and morphed (right figure) skin shapes.

The black line represents the average transition line on the upper surface, and its variation as function of the span-wise position can clearly be observed. The two dashed white lines represent the estimated extent of the transition region, determined as function of the chord-wise temperature gradient existing between laminar and turbulent regimes. The transition from laminar to turbulent flow occurs over a narrow region and it was automatically detected for the wing upper surface using a MATLAB code that was specifically developed for the IR images post-processing [44]. The red dot corresponds to the estimated transition in the span-wise section situated at 0.612 m from the root section (40% of the model span), that is half-way between the two Kulite piezoelectric pressure sensors lines. The accuracy of the transition detection for this section was estimated to ±2% of the local chord, based on the known Kulite positions and their thermal signatures in the images.

6. Results and discussion

6.1. The test cases

The two-dimensional aerodynamic optimizations that determined the electrical actuators displacements were performed with the objective of controlling the extent of laminar flow on the upper surface of the wing model.

These optimizations were performed for several flight conditions (expressed in terms of Mach number, Reynolds number and angle of attack) and several rigid aileron deflection angles. The cases that were optimized, analyzed and experimentally tested for laminar flow increase are presented in Table 3. The Reynolds numbers that correspond to the two Mach numbers are 4.28×10^6 and 5.27×10^6. A downwards aileron deflection was considered positive, while an upwards aileron deflection was considered as negative.

For each case, the transition point location on the pressure sensors line was determined from the numerical simulation and was compared to the experimentally measured transition location, determined using the IR thermography. The transition point location in the numerical results was determined by plotting the turbulence intermittency γ versus the local chord, for the upper and lower wing surfaces. In order to consistently extract the transition location, the first derivative of the intermittency plot was used. Since the intermittency is approximately constant for the laminar boundary layer and its value significantly increases in the transition region, the first derivative can be used to identify this region of high gradient. The transition point was considered to be the most upstream point where the derivative becomes non-zero. As an example, Fig. 12 shows the intermittency distribution at 0.612

Please cite this article in press as: O. Şugar Gabor et al., Numerical simulation and wind tunnel tests investigation and validation of a morphing wing-tip demonstrator aerodynamic performance, Aerosp. Sci. Technol. (2016), http://dx.doi.org/10.1016/j.ast.2016.03.014

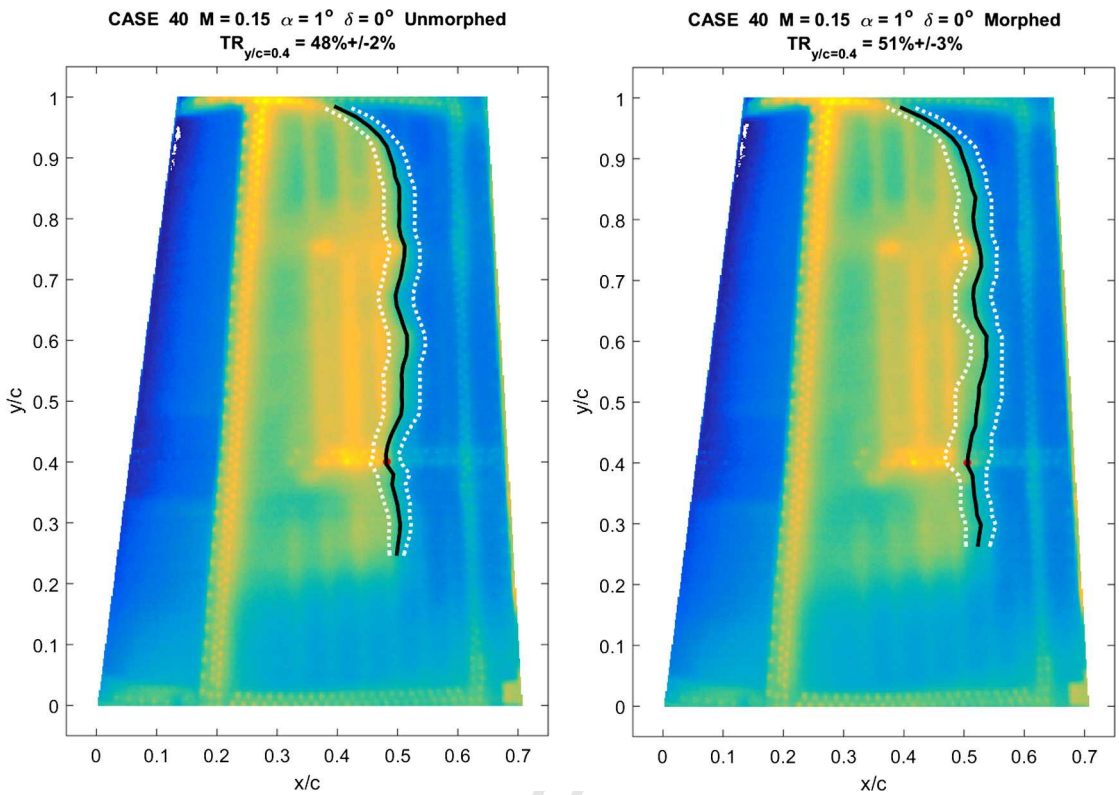

Fig. 11. IR visualization of the laminar-to-turbulent transition region on the upper surface for both un-morphed (left) and morphed (right) skin shapes. (For interpretation of the references to color in this figure, the reader is referred to the web version of this article.)

Table 3
Test cases optimized for laminar flow improvement.

Mach	Delta [°]	Angle of attack [°]										
		0	0.50	0.75	1.00	1.25	1.50	2.00	2.50	3.00	4.00	5.00
0.15	0	–	–	C39	C40	C41	C42	C43	C44	C45	–	–
0.20	4	C68	C69	–	C70	–	C71	C72	C73	–	–	–
0.20	−4	C74	C75	–	C76	–	C77	C78	C79	C80	C81	C82

m span-wise section, for case C39 un-morphed. The laminar-to-turbulent transition corresponds to the region of high gradient.

6.2. Upper surface transition location

Fig. 13 presents a comparison between the predicted and the measured transition location for the un-morphed and morphed wing upper surface skin, at a spanwise station corresponding to 40% of the wing span. The comparison shows both numerical and IR experimental results for cases C39 to C45 (Mach number of 0.15, no aileron deflection and angles of attack between 0.75 and 3°).

Fig. 14 displays the experimental transition location measurement compared to the numerical predictions for cases C68 to C73 (Mach number of 0.20, 4° downwards aileron deflection and angles of attack between 0 and 2.5°). No IR experimental data was available for case C68 (0° angle of attack).

In Fig. 15, the experimental and numerical transition location detection for cases C74 to C82 (Mach number of 0.20, 4° upwards aileron deflection and angles of attack between 0 and 5°) is presented for both un-morphed and morphed wing geometries. No IR experimental data was available for cases C74 (0° angle of attack) and C80 (3° angle of attack).

In Fig. 13, it can be seen that a reasonable agreement exists between the experimental and the numerically determined transition point location at the pressure sensors section for the un-morphed wing. For these cases (C39 to C45, with no aileron deflection), the

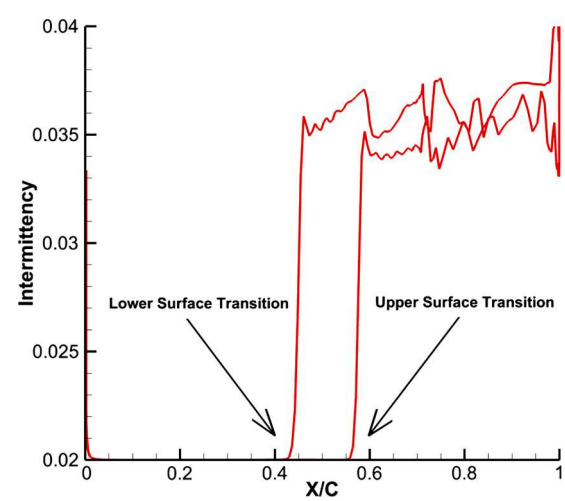

Fig. 12. Transition detection for Case 39 un-morphed using the turbulence intermittency distribution.

un-morphed wing error is around 5% of the local chord (corresponding to 0.05C in the figure). The IR experimental results show a successful improvement of laminar flow for the section of interest. The transition is delayed towards the trailing edge by 3–5% of the chord (equivalent to 0.03–0.05C in the figures). For the

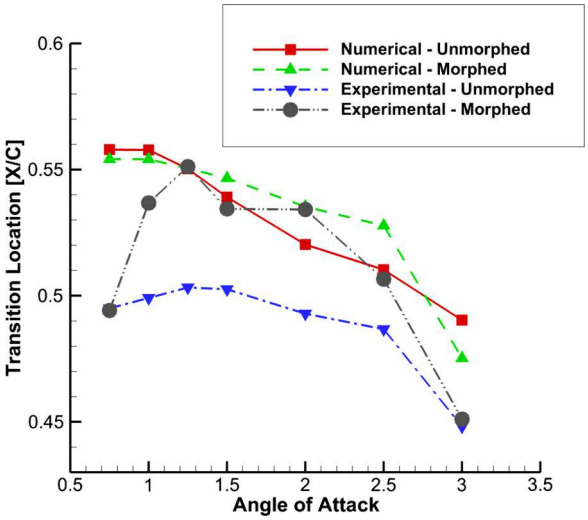

Fig. 13. Comparison between numerical and IR experimental transition detection for the station located at 40% of the span for the un-morphed and morphed wings of cases C39–C45.

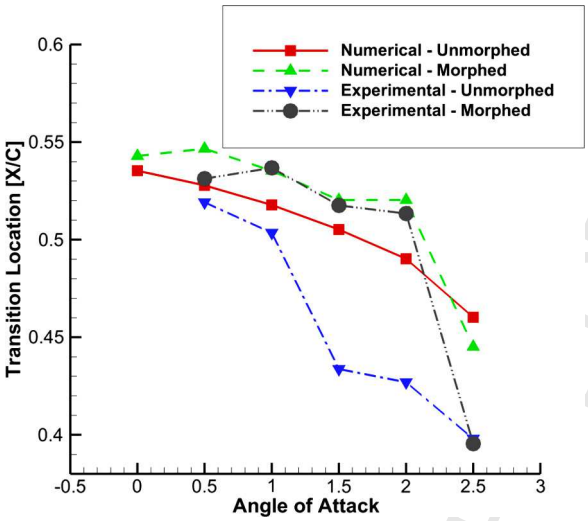

Fig. 14. Comparison between numerical and IR experimental transition detection for the station located at 40% of the span, for the un-morphed and morphed wings of cases C68–C73.

morphed geometries results presented in Fig. 13, the agreement between the numerical and IR transition positions is better than for the un-morphed wing, even though the predicted performance improvement is smaller.

In Fig. 14 (cases C68 to C73, having a 4° aileron deflection), for angles of attack smaller than 1°, there is a very good agreement between numerical versus experimental results obtained for the un-morphed wing. The discrepancy is seen to increase for angles of attack higher than 1.5°, as the experimental measurements show an early shift of the transition occurrence towards the wing leading edge. Again, a successful improvement of laminar flow is observed, with delays of 9% of the chord obtained for two angles of attack values (1.5° and 2°). The morphed geometries presented in Fig. 14 show a very good level of agreement between numerical and IR experimental results, with errors of maximum 2–3% of the chord (equivalent to 0.02–0.03C in the figure).

For cases C74 to C82 (−4° aileron deflection), presented in Fig. 15, there is a rather good agreement between the IR data and the numerical results for the un-morphed wing (transition position

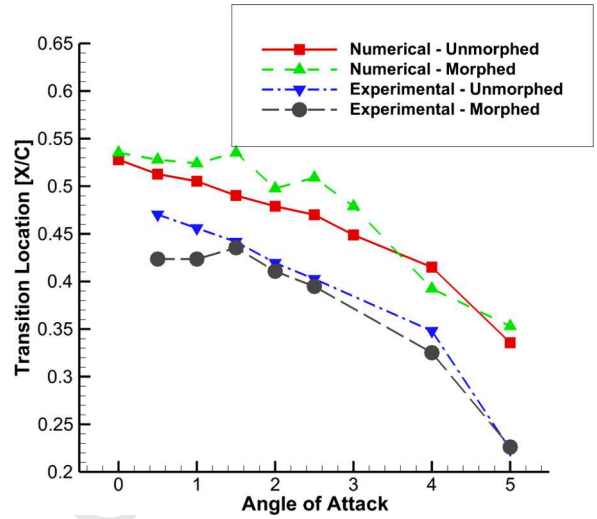

Fig. 15. Comparison between numerical and IR experimental transition detection for the station located at 40% of the span, for the un-morphed and morphed wings of cases C74–C82.

errors of around 5% of the chord), but the differences are higher for the morphed wing geometries. For the angles of attack between 1° and 3° the laminar flow delay predicted by the numerical results is not observed in the IR measurements.

Since all of the above presented results were obtained for the section located at 40% of the span, they only offer local information about the performance of the morphing upper skin. To provide a qualitative assessment of the skin's influence on the transition region for the entire upper surface, 2D plots are presented in Figs. 16 to 18, for cases C40 (Fig. 16), C72 (Fig. 17) and C77 (Fig. 18), respectively. These cases were chosen among those for which important transition location delays were observed on the pressure sensors span-wise section (as shown in Figs. 13 to 15), and they cover all three aileron deflection angles. This choice verification whether the extension of laminar flow was a phenomenon present on the entire upper surface, or if it was limited to a certain span-wise interval.

In the numerical results, the disturbances in transition position appearing near the wing root section were given by the 6.5 mm gap between the wing root rib and the symmetry plane. This gap was present in the experimental setup and included in the simulations. Its effect was not captured with the IR measurements due to the decrease in data quality in the region close to the wing root section.

For the wing tip region, the precision of the numerical simulations breaks down and an unrealistic laminar flow appears in all the results. This can be explained by the fact that the γ–$Re_{\theta t}$ model contains one empirical correlation for the transition onset that was calibrated especially for natural transition (stream-wise Tollmien–Schlichting instabilities) and laminar separation bubbles, while in reality the wing tip region is strongly contaminated by complex, cross-flow instabilities induced by the presence of the wing tip vortex.

An analysis of Figs. 16 to 18 shows that the behavior of the laminar flow region (under the actuation of the upper skin) that was observed from the pressure sensors line (indicated by the red dot in the experimental IR data and by the black line in the numerical results) can also be observed for other span-wise sections. Thus, when a successful transition delay was obtained for the pressure sensors line, this delay can be seen occurring not only locally but also over a high percentage of the wing's span, indicating the effectiveness of the upper surface morphing skin.

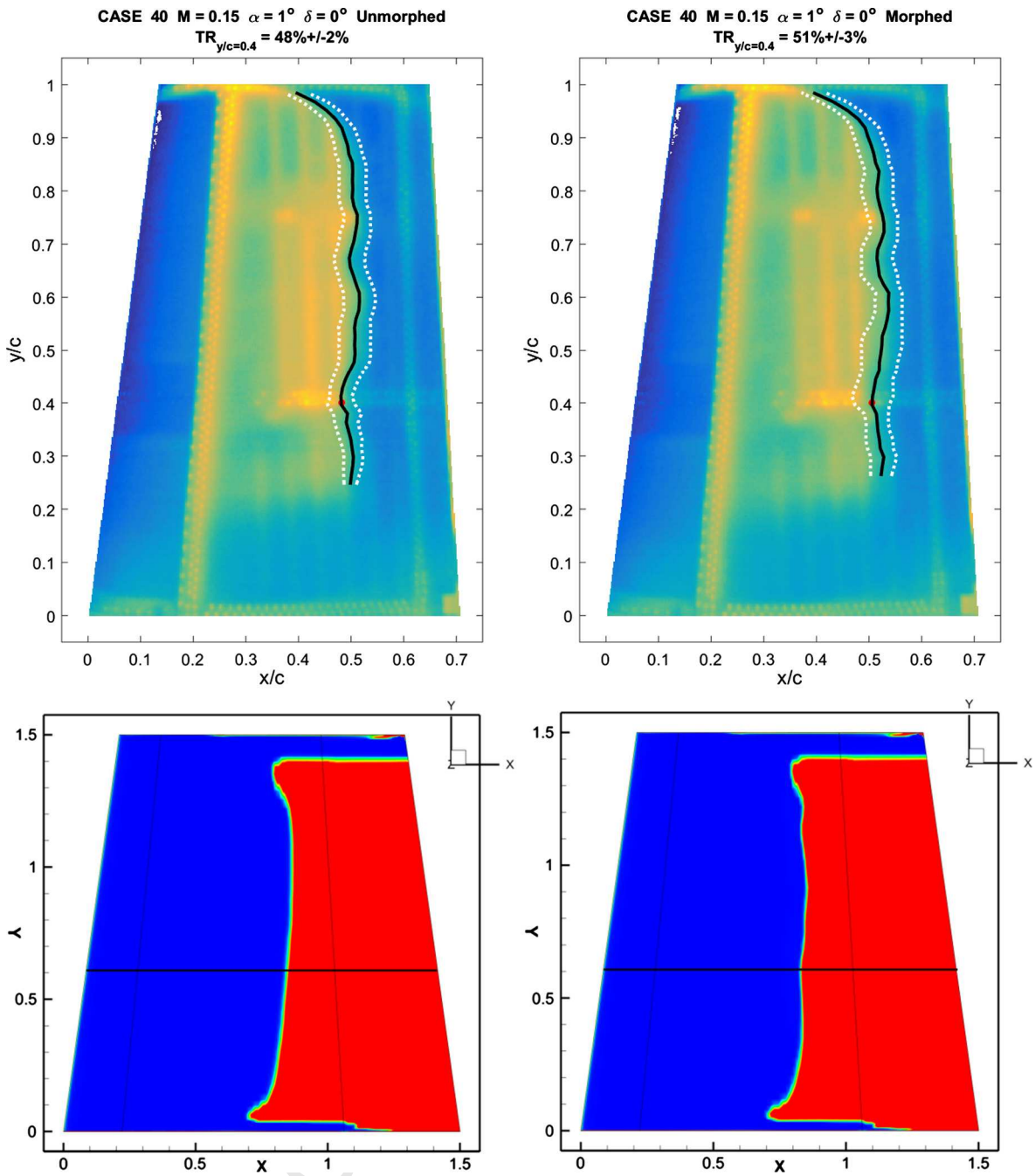

Fig. 16. Comparison between experimental and numerical transition location on the wing upper surface for case C40, for both un-morphed (left) and morphed (right) geometries. (For interpretation of the references to color in this figure, the reader is referred to the web version of this article.)

6.3. Pressure coefficient distribution comparisons

A comparison between the experimental and numerical pressure coefficient distributions for the section located at 40% of the wing span is presented in Figs. 19 to 22, for the following 4 cases: C40 (Mach number of 0.15, angle of attack of 1° and no aileron deflection), C68 (Mach number of 0.20, angle of attack of 0° and 4° aileron deflection) and for C79 and C82 (Mach number of 0.20, angles of attack of 2.5° and 5° and −4° aileron deflection).

Good agreement exits between numerical predictions and the wind tunnel measurements for the two sets of results given by case C40 and C68 (Figs. 19 and 20). The influence of the upper skin shape change can be observed from the differences between the un-morphed (left) and morphed (right) pressure coefficient distributions, for the chordwise interval between 25% and 60% of the chord. The skin morphing extends the region where the air accelerates over the upper surface, thus creating more favorable conditions for laminar flow, this effect being clearly visible in the two figures.

For cases C79 and C82 (shown in Figs. 21 and 22), a small difference exists in the upper surface pressure coefficient up to 50% of the chord, and very good agreement exists between the numerical and experimental results for the aileron, rigid lower skin and the upper surface downstream of 50% of the chord. Again, the influence of the morphing skin is clearly observable by comparing the left (un-morphed) and right (morphed) pressure distributions for the two figures.

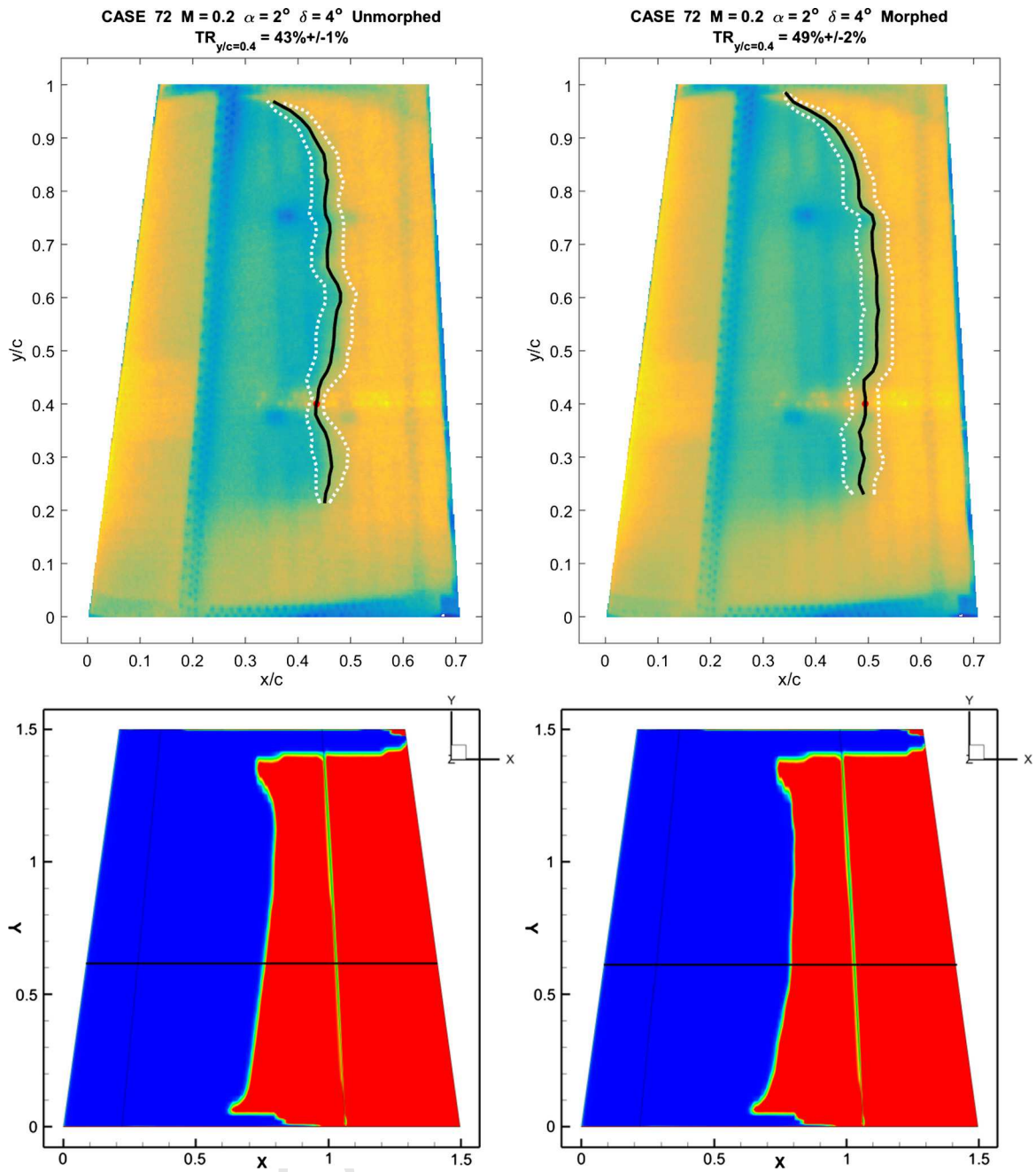

Fig. 17. Comparison between experimental and numerical transition location on the wing upper surface for case C72, for both un-morphed (left) and morphed (right) geometries. (For interpretation of the references to color in this figure, the reader is referred to the web version of this article.)

6.4. Aerodynamic coefficients comparison

In Tables 4 and 5, a comparison is made between the lift and drag coefficients for the un-morphed and morphed geometries, obtained through the numerical simulations and the experimental tests. The comparison is presented for cases C38 to C45, which were analyzed at a Mach number of 0.15 and had no aileron deflection.

The numerical lift coefficient values in Table 4 were found to be in good agreement with the experimental values included in Table 5, a small underestimation being observed for the 2.5 and 3° angles of attack. Concerning the drag coefficient, the numerical values are always under-predicted compared to the experimental ones, the average error being around 25%. The experimental drag coefficient data shows that the morphing of the upper surface skin caused a reduction of the wing model drag coefficient, with reductions between 0.20% and 0.60%, for all analyzed cases, while the numerical simulations did not capture this reduction. Table 6 shows the detailed differences obtained between the numerical and experimental coefficients.

Another comparison was done between the lift and drag coefficients obtained for the un-morphed and morphed geometries, through the numerical simulations and the experimental tests, and is presented in Tables 7 and 8. Cases C68 to C73, analyzed at a Mach number of 0.20 and with a 4° aileron deflection were included in the comparison. Details about the differences obtained between the numerical and experimental results are shown in Table 9.

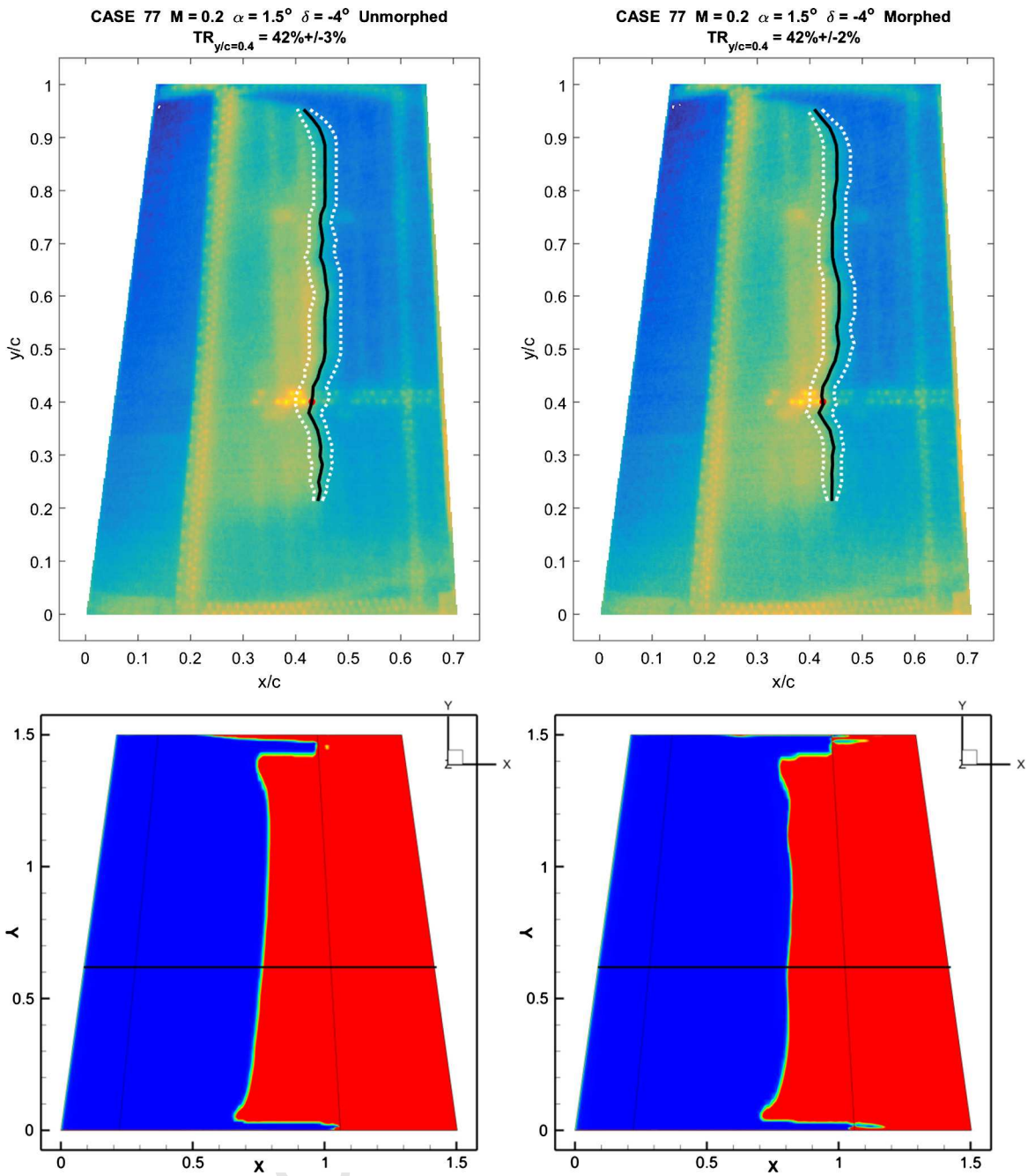

Fig. 18. Comparison between experimental and numerical transition location on the wing upper surface for case C77, for both un-morphed (left) and morphed (right) geometries. (For interpretation of the references to color in this figure, the reader is referred to the web version of this article.)

The qualitative behavior of the results remains the same as for cases C39 to C45. A good agreement between the experimental and numerical lift coefficients, and a 20–25% under-estimation of the numerically calculated drag, compared to the experimental values. The upper skin morphing determines 0.15–0.40% reduction of the wing drag coefficient, as confirmed by the results shown in Table 7. The numerically calculated drag coefficient for the morphed wing was higher than the value calculated for the un-morphed wing, thus not predicting the reduction effect observed experimentally.

Tables 10 and 11 show the comparison between the lift and drag coefficients for the un-morphed and morphed wing geometries, using the results that were obtained through the numerical simulations and the experimental test. This comparison is presented for cases C74 to C82, analyzed at a Mach number of 0.20 and an aileron deflection angle of $-4°$.

Concerning the comparison between the numerical and experimental results, the remarks made in the paragraph above also apply for cases C74 to C82. There is an under-estimation of the calculated drag coefficient, and there is a better agreement in the case of the lift. The impact of the upper surface skin morphing on the drag coefficient was not uniform. In some cases a slight reductions of up to 0.67% were obtained, while for others, an increase was obtained. These drag variations were present in both experimental and numerical results. Table 12 shows the detailed differences obtained between the numerical and experimental results.

6.5. General observations about the morphing concept

The drag coefficient reductions obtained following the wing tunnel experimental testing are relatively small. It must be noted

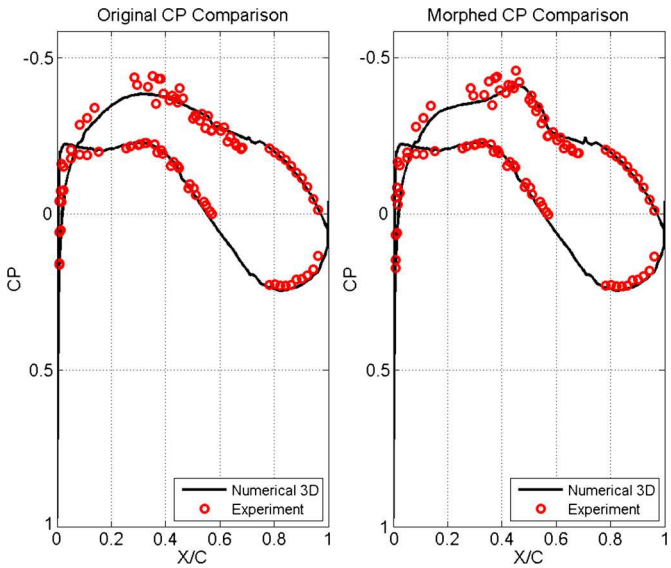

Fig. 19. Comparison of experimental versus numerical pressure coefficient distribution for case C40 corresponding to un-morphed (left) and morphed (right) wing.

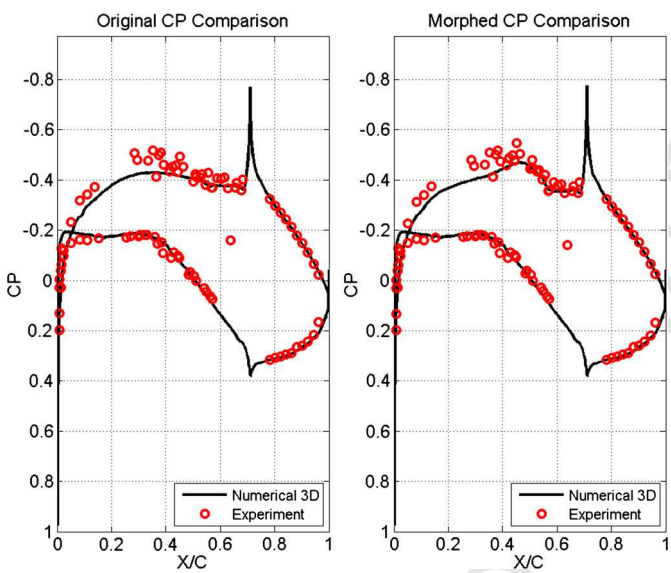

Fig. 20. Comparison of experimental versus numerical pressure coefficient distribution for case C68 corresponding to un-morphed (left) and morphed (right) wing.

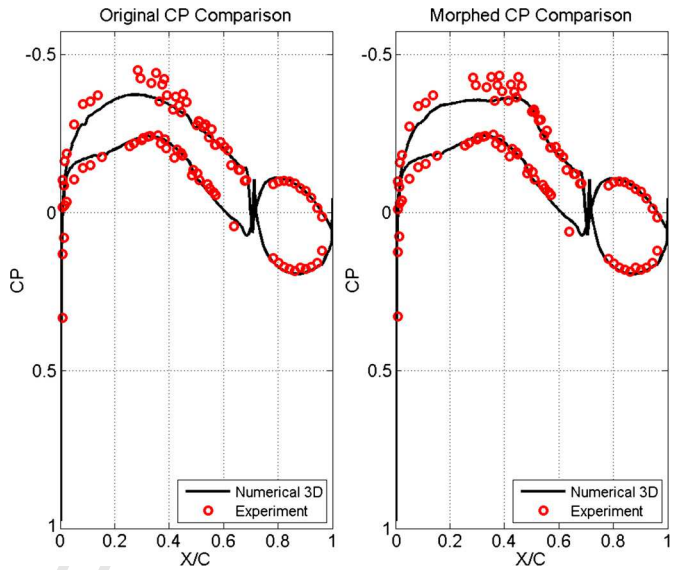

Fig. 21. Comparison of experimental versus numerical pressure coefficient distribution for case C79 corresponding to un-morphed (left) and morphed (right) wing.

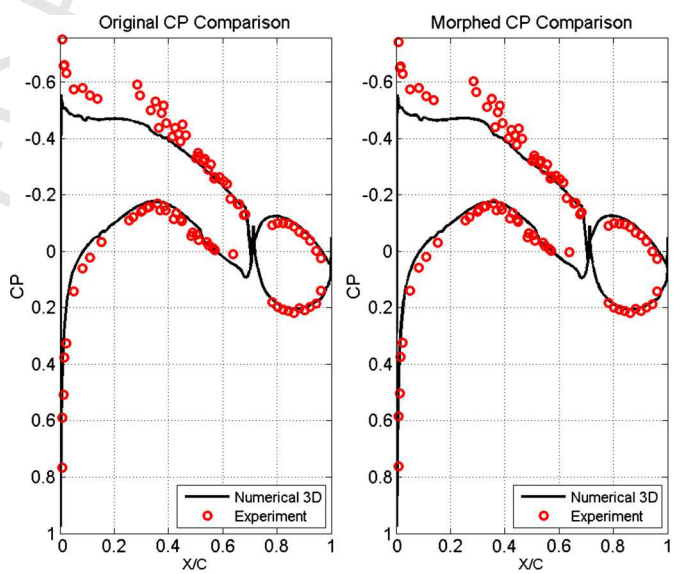

Fig. 22. Comparison of experimental versus numerical pressure coefficient distribution for case C82 corresponding to un-morphed (left) and morphed (right) wing.

that the aerodynamic loads balance that was used during testing was a very high precision instrument, with drag measurement uncertainties that were estimated to be of the order of 0.10–0.15% of the drag values. Thus, for the cases where the drag reduction between the morphed and un-morphed geometries was higher than the measurement error, the morphing upper surface has shown the ability of generating a small level of quantifiable improvements.

Upper skin morphing reduces the friction drag coefficient through the extension of the laminar flow region. Due to its very low aspect ratio, the wing model gives a poor performance in terms of the lift-induced drag, which has a much higher contribution to the total drag than in the case of a typical high aspect ratio wing (the complete wing of an aircraft). Thus, when the friction drags' percentage contribution to the total drag is higher (as, for example, a high aspect ratio wing during cruise flight), the drag reduction obtained by the concept could be higher.

During the design phase of the flexible composite skin, special attention was given to the reduction of the weight of upper surface, in comparison with the original aluminum design. This was achieved by varying the skin thickness as function of the local stress and by using composite material stringers (instead of the original aluminum stringers). The composite skin weight was more than 2 kg lighter than the original aluminum skin, and this weight reduction perfectly compensated the introduction of the 4 actuators inside the wing box, whose overall weight was approximately 2 kg. Thus, the difference in terms of weight between the non-morphing and morphing structure was negligible.

In the present multidisciplinary CRIAQ MDO 505 project, an industrial wing-tip was designed and morphed, and for this reason, several strict structural constraints and upper skin behavior uncertainties existed, which were added to the errors existing between numerical models/simulations and experimental results. Detailed tests must be performed in order to quantify the impact of the skin shape variations (differences between target and obtained shapes) on the quality of the laminar flow optimizations. In order to continue performing other types of research studies on upper surface morphing wings and aero-structural optimizations, it will be in-

Table 4
Comparison between the numerical un-morphed and morphed wing lift and drag coefficients for cases C39 to C45.

Numerical results						
Case	Angle of attack [°]	Un-morphed wing		Morphed wing		Drag variation [%]
		CL	CD	CL	CD	
C39	0.75	0.2058	0.0118	0.2059	0.0118	−0.01%
C40	1	0.2191	0.0126	0.2196	0.0126	0.24%
C41	1.25	0.2325	0.0134	0.2330	0.0134	0.18%
C42	1.50	0.2460	0.0142	0.2464	0.0142	0.10%
C43	2	0.2729	0.0161	0.2736	0.0161	0.19%
C44	2.50	0.3002	0.0183	0.3009	0.0183	0.13%
C45	3	0.3276	0.0206	0.3278	0.0206	0.18%

Table 5
Comparison between the experimental un-morphed and morphed wing lift and drag coefficients for cases C39 to C45.

Experimental results (loads balance measurements)						
Case	Angle of attack [°]	Un-morphed wing		Morphed wing		Drag variation [%]
		CL	CD	CL	CD	
C39	0.75	N/A	N/A	N/A	N/A	N/A
C40	1	0.2150	0.0156	0.2165	0.0156	−0.20%
C41	1.25	0.2324	0.0168	0.2329	0.0167	−0.47%
C42	1.50	0.2483	0.0180	0.2490	0.0178	−0.51%
C43	2	0.2794	0.0206	0.2788	0.0204	−0.60%
C44	2.50	0.3102	0.0235	0.3109	0.0234	−0.40%
C45	3	0.3434	0.0267	0.3424	0.0266	−0.23%

Table 6
Deltas between the numerical and experimental wing lift and drag coefficients for cases C39 to C45.

Case	Angle of attack [deg.]	Un-morphed wing		Morphed wing	
		ΔCL [$\cdot 10^{-2}$]	ΔCD [$\cdot 10^{-3}$]	ΔCL [$\cdot 10^{-2}$]	ΔCD [$\cdot 10^{-3}$]
C39	0.75	N/A	N/A	N/A	N/A
C40	1	−0.409	3.030	−0.305	2.968
C41	1.25	−0.015	3.412	−0.007	3.308
C42	1.50	0.228	3.753	0.257	3.648
C43	2	0.652	4.444	0.524	4.291
C44	2.50	0.999	5.220	1.001	5.101
C45	3	1.578	6.110	1.457	6.013

Table 7
Comparison between the numerical un-morphed and morphed wing lift and drag coefficients for cases C68 to C73.

Numerical results						
Case	Angle of attack [deg.]	Un-morphed wing		Morphed wing		Drag variation [%]
		CL	CD	CL	CD	
C68	0	0.2990	0.0191	0.2994	0.0191	0.03%
C69	0.5	0.3254	0.0212	0.3260	0.0212	0.07%
C70	1	0.3519	0.0236	0.3527	0.0237	0.19%
C71	1.5	0.3783	0.0263	0.3780	0.0263	0.13%
C72	2	0.4047	0.0292	0.4057	0.0292	0.15%
C73	2.5	0.4318	0.0323	0.4300	0.0322	−0.09%

Table 8
Comparison between the experimental un-morphed and morphed wing lift and drag coefficients for cases C68 to C73.

Experimental results (loads balance measurements)						
Case	Angle of attack [deg.]	Un-morphed wing		Morphed wing		Drag variation [%]
		CL	CD	CL	CD	
C68	0	0.3023	0.0231	0.3034	0.0230	−0.15%
C69	0.5	0.3350	0.0261	0.3358	0.0260	−0.36%
C70	1	0.3671	0.0295	0.3671	0.0294	−0.41%
C71	1.5	0.3996	0.0333	0.3999	0.0332	−0.15%
C72	2	0.4318	0.0373	0.4329	0.0372	−0.26%
C73	2.5	0.4660	0.0417	0.4634	0.0416	−0.25%

Please cite this article in press as: O. Şugar Gabor et al., Numerical simulation and wind tunnel tests investigation and validation of a morphing wing-tip demonstrator aerodynamic performance, Aerosp. Sci. Technol. (2016), http://dx.doi.org/10.1016/j.ast.2016.03.014

Table 9
Deltas between the numerical and experimental wing lift and drag coefficients for cases C68 to C73.

Case	Angle of attack [deg.]	Un-morphed wing		Morphed wing	
		ΔCL [$\cdot 10^{-2}$]	ΔCD [$\cdot 10^{-3}$]	ΔCL [$\cdot 10^{-2}$]	ΔCD [$\cdot 10^{-3}$]
C68	0	0.329	3.954	0.397	3.914
C69	0.5	0.963	4.922	0.980	4.813
C70	1	1.516	5.892	1.437	5.726
C71	1.5	2.132	6.960	2.093	6.878
C72	2	2.708	8.117	2.718	7.979
C73	2.5	3.412	9.447	3.335	9.373

Table 10
Comparison between the numerical un-morphed and morphed wing lift and drag coefficients for cases C74 to C82.

Numerical results						
Case	Angle of attack [deg.]	Un-morphed wing		Morphed wing		Drag variation [%]
		CL	CD	CL	CD	
C74	0	0.0206	0.0061	0.0208	0.0061	−0.13%
C75	0.5	0.0461	0.0063	0.0461	0.0062	−0.28%
C76	1	0.0716	0.0064	0.0718	0.0065	0.67%
C77	1.5	0.0967	0.0069	0.0963	0.0070	0.20%
C78	2	0.1222	0.0077	0.1227	0.0076	−0.51%
C79	2.5	0.1477	0.0086	0.1470	0.0085	−0.34%
C80	3	0.1733	0.0098	0.1738	0.0097	−0.44%
C81	4	0.2250	0.0128	0.2243	0.0128	0.01%
C82	5	0.2765	0.0168	0.2766	0.0168	−0.05%

Table 11
Comparison between the experimental un-morphed and morphed wing lift and drag coefficients for cases C74 to C82.

Experimental results (loads balance measurements)						
Case	Angle of attack [deg.]	Un-morphed wing		Morphed wing		Drag variation [%]
		CL	CD	CL	CD	
C74	0	0.0082	0.0083	0.0082	0.0083	0.04%
C75	0.5	0.0383	0.0084	0.0382	0.0084	−0.09%
C76	1	0.0679	0.0088	0.0680	0.0088	0.33%
C77	1.5	0.0983	0.0094	0.0992	0.0095	0.76%
C78	2	0.1294	0.0105	0.1230	0.0105	0.09%
C79	2.5	0.1602	0.0119	0.1560	0.0119	−0.14%
C80	3	0.1917	0.0137	0.1912	0.0136	−0.67%
C81	4	0.2531	0.0182	0.2541	0.0183	0.59%
C82	5	0.3175	0.0241	0.3171	0.02401	−0.03%

Table 12
Errors between the numerical and experimental wing lift and drag coefficients for cases C74 to C82.

Case	Angle of attack [deg.]	Un-morphed wing		Morphed wing	
		ΔCL [$\cdot 10^{-2}$]	ΔCD [$\cdot 10^{-3}$]	ΔCL [$\cdot 10^{-2}$]	ΔCD [$\cdot 10^{-3}$]
C74	0	−1.241	2.078	−1.252	2.089
C75	0.5	−0.774	2.132	−0.788	2.142
C76	1	−0.369	2.349	−0.381	2.334
C77	1.5	0.158	2.452	0.284	2.510
C78	2	0.726	2.784	0.730	2.832
C79	2.5	1.252	3.267	1.274	3.279
C80	3	1.845	3.876	1.737	3.828
C81	4	2.813	5.362	2.981	5.467
C82	5	4.102	7.307	4.047	7.308

teresting to study other multidisciplinary approaches, as the ones defined in [45].

The experimental tests and results obtained up to this day and presented in this paper included only the wing model equipped with the rigid aileron. The CRIAQ MDO 505 project will continue by performing the numerical studies and experimental tests on the morphing aileron. The aim will be to realize the proof of concept, where the new morphing aileron design would require lower deflection angles in order to provide the same degree of roll authority as the rigid aileron.

7. Conclusions

The results obtained using CFD numerical simulation and experimental wind tunnel testing for a morphing wing equipped with a flexible upper surface and controllable rigid aileron were presented. The morphing wing tip was manufactured and fitted with a composite material upper skin. Two-dimensional optimizations were performed with the aim of controlling the extent of the laminar flow region, and the resulting skin shapes were scanned using high-precision photogrammetry. A grid convergence study was per-

formed to determine the optimal mesh refinement required by the numerical transition model. Subsonic wind tunnel tests were performed at the NRC 2 m × 2 m wind tunnel, and the experimental measurements included Infra-Red thermography, pressure sensors measurements and balance loads measurements.

Three series of cases were analyzed, each consisting of a sweep over a range of angles of attack, at a constant Mach number and aileron deflection angle. Comparisons were made between the un-morphed and morphed upper skin shapes, for the transition point location at the station situated at 40% of the wing span, corresponding to the pressure sensors station. Good agreement was obtained between the numerical and IR results, with an average prediction error of approximately 5% of the chord. Both the IR measurements and the numerical results have shown that an increase in the laminar flow region was obtained after the optimization. The experimental transition delay was between 3 and 9% of the chord, while the numerical improvements were smaller. The laminar flow extension was obtained for a significant percentage of the upper skin span. Pressure coefficient comparisons were performed at the 40% of the span section, and a good match was obtained. The lift and drag coefficients were determined for all 22 cases analyzed, for both un-morphed and morphed geometries. The force balance results show reductions of the drag coefficient of up to 0.67%. The numerical results predictions obtained with the chosen turbulence and transition models do not appear to be accurate enough to capture this drag reduction.

Conflict of interest statement

None declared.

Acknowledgements

We would like to express our appreciation for the financial support and contribution obtained from our industrial partners Bombardier Aerospace and Thales Canada, in the framework of the CRIAQ MDO 505 project. We also wish to thank NSERC for their financial support. Special thanks are due to our collaborators and leaders in this project: Mr. Patrick Germain and Mr. Fassi Kafyeke from Bombardier Aerospace, Mr. Philippe Molaret from Thales Canada, Mr. Eric Laurendeau from Ecole Polytechnique, and Mr. Erik Sherwood and his team from DFS-NRC for the design and fabrication of the wind tunnel model.

References

[1] ATAG, Aviation: benefits without borders, Report, 2014, Air Transport Action Group, http://www.atag.org/.
[2] ICAO, Aviation's contribution to climate change, Environmental report, 2010, International Civil Aviation Organisation, http://www.icao.int/.
[3] S. Barbarino, O. Bilgen, R.M. Ajaj, M.I. Friswell, D.J. Inman, A review of morphing aircraft, J. Intell. Mater. Syst. Struct. 22 (9) (2011) 823–877.
[4] P. Gamboa, P. Alexio, J. Vale, F. Lau, A. Suleman, Design and testing of a morphing wing for an experimental UAV, RTO-MP-AVT-146, Neuilly-sur-Seine, France, 2007.
[5] J. do Vale, A. Leite, F. Lau, A. Suleman, Aero-structural optimization and performance evaluation of a morphing wing with variable span and camber, J. Intell. Mater. Syst. Struct. 22 (10) (2011) 1057–1073.
[6] L. Falcao, A.A. Gomes, A. Suleman, Aero-structural design optimization of a morphing wingtip, J. Intell. Mater. Syst. Struct. 22 (10) (2011) 1113–1124.
[7] G. Diodati, A. Concilio, S. Ricci, A. De Gaspari, C. Liauzun, J.L. Godard, Estimated performance of an adaptive trailing-edge device aimed at reducing fuel consumption on a medium-size aircraft, in: 8690-14, Smart Structures/NDE Conference, 10–14 March 2013, San Diego, CA, USA.
[8] R. Pecora, F. Amoroso, G. Amendola, A. Concilio, Validation of a smart structural concept for wing-flap camber morphing, Smart Struct. Syst. 14 (4) (2014) 659–678.
[9] R. Pecora, F. Amoroso, L. Lecce, Effectiveness of wing twist morphing in roll control, J. Aircr. 49 (6) (2012) 1666–1674.
[10] D.R. Bye, P.D. McClure, Design of a morphing vehicle, in: Proceedings of 48th AIAA/ASME/ASCE/AHS/ASC Structures, Structural Dynamics and Materials Conference, 23–26 April 2007, Honolulu, HI, AIAA 2007-1728.
[11] T.G. Ivanco, R.C. Scott, M.H. Love, P.S. Zink, T.A. Weisshaar, Validation of the Lockheed Martin morphing concept with wind tunnel testing, in: Proceedings of 48th AIAA/ASME/ASCE/AHS/ASC Structures, Structural Dynamics and Materials Conference, 23–26 April 2007, Honolulu, HI, AIAA 2007-2235.
[12] M.H. Love, P.S. Zink, R.L. Stroud, D.R. Bye, S. Rizk, D. White, Demonstration of morphing technology through ground and wind tunnel tests, in: Proceedings of 48th AIAA/ASME/ASCE/AHS/ASC Structures, Structural Dynamics and Materials Conference, 23–26 April 2007, Honolulu, HI, AIAA 2007-1729.
[13] G.R. Andersen, D.L. Cowan, D.J. Piatak, Aeroelastic modeling, analysis and testing of a morphing wing structure, in: Proceedings of 48th AIAA/ASME/ASCE/AHS/ASC Structures, Structural Dynamics and Materials Conference, 23–26 April 2007, Honolulu, HI, AIAA 2007-1734.
[14] J.S. Flanagan, R.C. Strutzenberg, R.B. Myers, J.E. Rodrian, Development and flight testing of a morphing aircraft, the NextGen MFX1, in: Proceedings of 48th AIAA/ASME/ASCE/AHS/ASC Structures, Structural Dynamics and Materials Conference, 23–26 April 2007, Honolulu, HI, AIAA 2007-1707.
[15] D.D. Smith, M.H. Lowenberg, D.P. Jones, M.I. Friswell, Computational and experimental validation of the active morphing wing, J. Aircr. 51 (3) (2014) 925–937.
[16] J.E. Murray, J.W. Pahle, S.V. Thornton, S. Vogus, T. Frackowiak, J.D. Mello, B. Norton, Ground and flight evaluation of a small scale inflatable winged aircraft, in: 40th AIAA Aerospace Sciences Meeting and Exhibition, Reno, NV, USA, AIAA Paper 2002-0820.
[17] D.A. Neal, M.G. Good, C.O. Johnston, H.H. Robertshaw, W.H. Mason, D.J. Inman, Design and wind tunnel analysis of a fully adaptive aircraft configuration, in: 45th AIAA/ASME/ASCE/AHS/ASC Structures, Structural Dynamics and Materials Conference, 19–22 April 2004, Palm Springs, CA, AIAA 2004-1727.
[18] R. Pecora, S. Barbarino, A. Concilio, L. Lecce, S. Russo, Design and functional test of a morphing high-lift device for a regional aircraft, J. Intell. Mater. Syst. Struct. 22 (10) (2011) 1005–1023.
[19] O. Bilgen, K.B. Kochersberger, E.C. Diggs, A.J. Kurdila, D.J. Inman, Morphing wing micro-air-vehicles via macro-fiber-composite actuators, in: Proceedings of 48th AIAA/ASME/ASCE/AHS/ASC Structures, Structural Dynamics and Materials Conference, 23–26 April 2007, Honolulu, HI, AIAA Paper 2007-1785.
[20] O. Bilgen, K.B. Kochersberger, D.J. Inman, Macro-fiber composite actuator for a swept wing unmanned aerial vehicle, in: Special issue on Flight Structures Fundamental Research in the USA, 113 (2009) 385–395.
[21] A.M. Pankonien, D.J. Inman, Spanwise morphing trailing edge on a finite wing, in: Active and Passive Smart Structures and Integrated Systems 2015 Conference, San Diego, CA, USA, 8 March 2015.
[22] R.M. Botez, P. Molaret, E. Laurendeau, Laminar flow control on a research wing: project presentation covering a three-year period, in: Canadian Aeronautics and Space Institute Annual General Meeting, January 2007.
[23] V. Brailovski, P. Terriault, D. Coutu, T. Georges, E. Morellon, C. Fischer, S. Berube, Morphing laminar wing with flexible extrados powered by shape memory alloy actuators, in: Proceedings of SMASIS08 ASME Conference on Smart Materials, Adaptive Structures and Intelligent Systems, Ellicott City, Maryland, USA, 2008.
[24] L. Pages, O. Trifu, I. Paraschivoiu, Optimized laminar flow control on an airfoil using the adaptable wall technique, in: Proceedings of the Canadian Aeronautics and Space Institute Annual General Meeting, Toronto, Canada, 2007.
[25] A.V. Popov, L. Grigorie, R.M. Botez, M. Mamou, Y. Mebarki, Modeling and testing of a morphing wing in an open loop architecture, AIAA J. Aircr. 47 (3) (2010) 917–923.
[26] T.L. Grigorie, A.V. Popov, R.M. Botez, Adaptive neuro-fuzzy controllers for an open loop morphing wing system, Proc. Inst. Mech. Eng., Part G, J. Aerosp. Eng. 223 (7) (2009) 965–975.
[27] A.V. Popov, L. Grigorie, R.M. Botez, M. Mamou, Y. Mebarki, Real time airfoil optimisation of a morphing wing in a wind tunnel, AIAA J. Aircr. 47 (4) (2010) 1346–1354.
[28] A.V. Popov, L. Grigorie, R.M. Botez, M. Mamou, Y. Mebarki, Closed loop control of a morphing wing in a wind tunnel, AIAA J. Aircr. 47 (4) (2010) 1309–1317.
[29] T.L. Grigorie, A.V. Popov, R.M. Botez, M. Mamou, Y. Mebarki, On-off and proportional-integral controller for morphing wing. Part 1: actuation mechanism and control design, Proceedings of the Institution of Mechanical Engineers, Part G J. Aerosp. Eng. 226 (2) (2012) 131–145.
[30] T.L. Grigorie, A.V. Popov, R.M. Botez, M. Mamou, Y. Mebarki, On-off and proportional-integral controller for morphing wing. Part 2: control validation, numerical simulations and experimental tests, Proc. Inst. Mech. Eng., Part G, J. Aerosp. Eng. 226 (2) (2012) 146–162.
[31] T.L. Grigorie, R.M. Botez, A.V. Popov, M. Mamou, Y. Mébarki, A hybrid fuzzy logic proportional-integral-derivative and conventional on-off controller for morphing wing actuation using shape memory alloy, part 1: morphing system mechanisms and controller architecture design, Aeronaut. J. 116 (1179) (2012) 433–449.
[32] T.L. Grigorie, R.M. Botez, A.V. Popov, M. Mamou, Y. Mébarki, A hybrid fuzzy logic proportional-integral-derivative and conventional on-off controller for morphing wing actuation using shape memory alloy, part 2: controller implementation and validation, Aeronaut. J. 116 (1179) (2012) 451–465.

[33] C. Sainmont, I. Paraschivoiu, D. Coutu, V. Brailovski, E. Laurendeau, M. Mamou, Y. Mebarki, M. Khalid, Boundary layer behaviour on an morphing wing: simulation and wind tunnel tests, in: Canadian Aeronautics and Space Institute AERO09 Conference, Toronto, Canada, 2009.

[34] T.L. Grigorie, R.M. Botez, A.V. Popov, Design and experimental validation of a control system for a morphing wing, in: AIAA Atmospheric Flight Mechanics Conference, Minneapolis, USA, August 2012.

[35] F. Michaud, Design and optimization of a composite skin for an adaptive wing, Master of Science Thesis, Ecole de technologie superieure, Montreal, Canada, 2014.

[36] F.R. Menter, Two-equation eddy-viscosity turbulence models for engineering applications, AIAA J. 32 (8) (1994) 1598–1605.

[37] R.B. Langtry, F.R. Menter, Correlation-based transition modeling for unstructured parallelized computational fluid dynamics codes, AIAA J. 47 (12) (2009) 2894–2906.

[38] ANSYS FLUENT, www.ansys.com.

[39] M. Drela, XFOIL: an analysis and design system for low Reynolds number airfoils, in: Low Reynolds Number Aerodynamics, Springer, 1989.

[40] A. Koreanschi, O. Sugar Gabor, R.M. Botez, New numerical study of boundary layer behaviour on a morphing wing-with-aileron system, American Institute of Aeronautics and Astronautics AIAA 32nd Applied Aerodynamics Conference, Atlanta, GA, USA, 16–20 June, 2014.

[41] A. Koreanschi, O. Sugar Gabor, R.M. Botez, Drag optimization of a wing equipped with a morphing upper surface, Aeronaut. J. (2016), in press.

[42] Y. Mebarki, T. Kameya, Optical real-time tracking using passive markers in the NRC 1.5M wind tunnel: application to the wind tunnel testing of stores release from an internal weapons bay, NRC LTR AL-2014-0042, 2014.

[43] Kulite Semiconductor Products, http://kulite.com/.

[44] Y. Mebarki, M. Mamou, M. Genest, Infrared measurements of the transition detection on the CRIAQ project morphing wing model, NRC LTR AL-2009-0075, 2009.

[45] J.R.R.A. Martins, A.B. Lambe, Multidisciplinary design optimization: a survey of architectures, AIAA J. 51 (9) (2013) 2049–2075.